UNIVERSITY OF CALIFORNIA, SAN DIEGO

Roles of 3D Traction Forces in Migration and Focal Adhesion Dynamics of Bovine Aortic Endothelial Cells

A dissertation submitted in partial satisfaction of the requirements for the degree

Doctor of Philosophy

in

Materials Science and Engineering

by

Sung-Sik Hur

Committee in charge:

Professor Shu Chien, Chair
Professor Sungho Jin, Co-Chair
Professor Sangeeta Bhatia
Professor Yuan-Cheng Fung
Professor Yu-Hwa Lo

2007

The dissertation of Sung-Sik Hur is approved, and it is acceptable in quality and form for publication on microfilm:

_____

_____

_____

_____

Co-chair

_____

Chair

University of California, San Diego

2007

DEDICATION

To My Wife Soh-Min Stephana Yee

and

To the Memory of My Father Tae-Uk Matthias Hur,

and My Mother Byung-Ae Stephana Kim

You Always Live in My Heart ….

TABLE OF CONTENTS

LIST OF FIGURES AND TABLES

ACKNOWLEDGMENTS

I would like to highly appreciate Professor Shu Chien for his remarkable guidance, support, patience, and advices. Not only as a researcher but also as a respectable human being, he has shown the model of the life. I want to give my special thanks to Dr. Yihua Zhao, Dr. Julie Li, and Dr. Shunichi Usami for their valuable support and guidance as mentors. Without their tremendous help, this work would not have been possible.

I would like to express my special thanks to Dr. Sungho Jin who provided valuable advices as a co-advisor, Dr. Yuan-Cheng Fung for his advices about stress analysis, Dr. Yu-Hwa Lo for his advices and helps, and Dr. Sangeeta Bhatia for her suggestions and kind helps.

I would like to appreciate to all my colleagues at UCSD: Dr. Troy Hornberger, Dr. Jason Haga, Dr. Annie Shou, Mr. Yingli Hu, Ian Lian, Joanne Chang, Leona Flores, Dan Fero, Dayu Teng, Angela Young, Mark Wang who have provided valuable support and discussions; Phu Nguyen, Jerry Norwich, and Suli Yuan who have given excellent assistance in conducting experiments.

Special gratitude goes to Dr. Sah, Dr. Chen, and Van Wang in the Dr. Sah Lab for the support and advices for the experiment to measure the mechanical properties. I want to thank to Dr. Hyunjung Yang and Dr. Jongkook Hong for the valuable advices and discussion for the finite element analysis.

Finally I thank my family who supported me in every step of my life and made these efforts meaningful. I want to thank my four elder sisters, Dr. JungHwa Hur, Su-Yeon Hur, Oak-Ryon Hur and Seung-Yeon Hur. I also appreciate the support from my parents in law Dr. Jong-Nyool Yee and HeeKyoung Cho and my brother and sister in law Gun-Woo Yee and Kyung-Min Yee. Finally I want to thank to my cute nephew and nieces Su-Ji Choi, Young-Kyun Shin, Seung-Kyun Shin, and Dong-Hoon Ko.

VITA

1971	Born, Jeonju City, South Korea
1994	B.S., Materials Science and Engineering (Fiber and Polymer Science), College of Engineering, Seoul National University, Seoul, South Korea
1995	Military Service (Forest Fire Agent), WanSan-Gu Office, Jeonju City, South Korea
1995-1998	M.S. Materials Science and Engineering (Fiber and Polymer Science), College of Engineering, Seoul National University, Seoul, South Korea
1999	Research Scientist, Chemical Engineering, College of Engineering, MyongJi Uiniversity, Yongin City, South Korea
2000-2007	Ph.D., Materials Science and Engineering program (Bioengineering), Jacobs School of Engineering, University of California, San Diego

ABSTRACT OF THE DISSERTATION

Roles of 3D Traction Forces in Migration and Focal Adhesion Dynamics of Bovine Aortic Endothelial Cells

by

Sung-Sik Hur

Doctor of Philosophy in Materials Science and Engineering

University of California, San Diego, 2007

Professor Shu Chien, Chair

Professor Sungho Jin, Co-Chair

Mechanical forces play an important role in the regulation of physiological responses which affect cell structure and function, including local changes of adhesion sites and cytoskeletons, and alterations in cell motility, proliferation and survival. The traction forces exerted by an adherent cell on the substrate have been studied with traction force microscopy techniques. However,

only two dimensional (2D) traction forces tangential to the substrate have been considered in the previous studies although forces are generally three-dimensional (3D) in nature.

I have developed a novel technique to measure 3D traction forces, including the normal forces as well as tangential forces, exerted by cultured bovine aortic endothelial cells (BAECs) based on the image processing techniques and finite element method (FEM).

Using this method, it has been demonstrated that not only tangential but also normal traction forces are related to the BAEC on the substrate. Upward normal traction force is shown at the edge of the BAEC while downward normal traction force is dominant under the nucleus.

Combined with green fluorescent protein (GFP) technique to visualize the focal adhesion (FA) molecules including focal adhesion kinase (FAK) and paxillin, it has been demonstrated that 3D traction force is related to the FA dynamics of BAECs. It has been shown in migrating cells that upward normal traction force is related to the dynamic FAs (FAs that traverse a long distance or undergo turnover), and that downward normal traction force is related to the stable FAs (FAs do not change their position and size).

This 3D traction force microscopy technique applied to BAECs and other types of cells provides a new way of assessing the full range of biomechanical dynamics of cells in conjunction with their biochemical activities and can contribute to the understanding of cellular functions in health and disease.

I. INTRODUCTION

Cells are constantly exposed to mechanical forces from either their own contractile machinery or various surrounding factors. These forces mediate the communication between cells and their surroundings, including neighboring cells and extracellular matrix (ECM). Recent studies have demonstrated that such mechanical forces play an important role in the regulation of physiological responses which affect cell structure and function, including local changes of adhesion sites and cytoskeletons, and alterations in cell motility, proliferation and survival (Bershadsky, Balaban et al. 2003; Vogel and Sheetz 2006).

Mechanical forces generated by cytoskeletal contraction, as well as the externally applied forces, can be the cause of cellular responses; the cellular responses, in turn, can generate mechanical forces, which then become the result. Mechanical forces, including the traction force generated by cytoskeletal contraction, can be the cause of a variety of cellular responses, e.g., proliferation (Nelson, Jean et al. 2005). Cells generate stronger traction forces on stiff substrate than on soft substrate (Shemesh, Geiger et al. 2005), indicating that different contractile force patterns generated by cells can result from differential responses to the physical aspects of the surroundings.

Recent developments in traction force microscopy have resulted in several new approaches for the detection of force generated by cultured cells. Combined with other approaches, such as green-fluorescent protein (GFP) imaging and gene manipulation, traction force microscopy proves to be powerful for analyzing the mechanical interplay between the cell and its environments (Beningo, Lo et al. 2002).

To date, however, only traction forces tangential to the substrate have been studied, although forces are generated in all three-dimensions (3D). Therefore, there is a need to investigate the traction forces generated by the cell in 3D, i.e., including the Z-drection. In this thesis, a novel

approach has been developed to determine traction force in the Z-direction, and the results have been correlated with cellular behaviors such as cell migration and focal adhesion (FA) dynamics.

1.1. Vascular Endothelial Cells

Vascular endothelial cells (ECs) are squamous layer of cells which form the inner lining of blood vessels (Fig. 1-1). In addition to serving as a permeability barrier, ECs perform many important functions, e.g., cell migration, remodeling, proliferation, apoptosis, and the production, secretion, and metabolism of biochemical substances, as well as the regulation of contractility of vascular smooth muscle cells. Besides their modulation by chemical ligands (e.g., growth factors and hormones), ECs also respond to mechanical factors, including the normal stress that result from the action of pressure and the shear stress due to flow. The control of intracellular mechanics and signaling in response to the external physical and chemical stimuli serves to maintain homeostasis at the cellular level, which is required for normal endothelial functions and protection against pathophysiological changes such as atherosclerosis (Chien 2007). ECs play a crucial role in vascular remodeling during angiogenesis and wound healing of vessel wall after denudation of ECs by balloon angioplasty or bypass surgery.

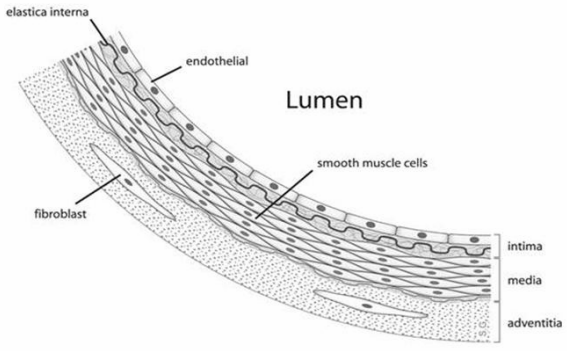

Fig. 1-1. Anatomy of the arterial wall
(http://en.wikipedia.org/wiki/Image)

The major aim of this study is to elucidate the role of the 3-D traction forces in the migration

of vascular ECs and relate the mechanical forces to dynamical changes in focal adhesion proteins during migration.

1.2. Focal Adhesions

The focal adhesions (FAs) or focal contacts are the subcellular sites where cytoskeletal and external forces act between cells and ECM. FAs are large, multiple intracellular anchor protein complex, including α-actinin, filamin, vinculin, talin, paxillin, and focal adhesion kinase (FAK), etc. (more than 50 different proteins).

In these regions, the cytoskeletons are connected to the ECM via the heterodimeric transmembrane receptors, i.e., integrins. The stress fibers (actin+myosin II filaments) terminate at these FAs sites (Fig. 1-2). The distance between the bottom of the adherent cell and the top of the substrate is about 10~15 μm at FAs, as compared with about 50 μm for non-FA sites (Alberts, 2002).

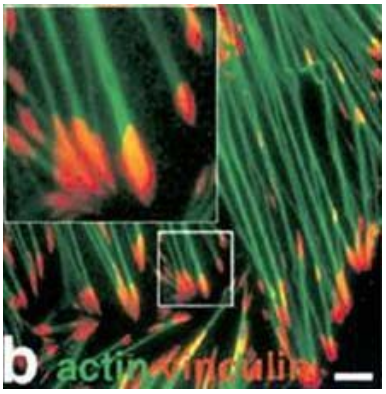

Fig. 1-2. Immunofluorescence microscopy of FA structure
Red=FAs, Green=Actin, Bar = 3μm (Zaidel-Bar, Cohen et al. 2004)

FAs provide mechanical links between the intracellular stress fibers with the ECM, and are major sites of force bearing (Fig. 1-3). Hence, FAs should be considered in investigating the transmission of traction forces from the cell to the ECM.

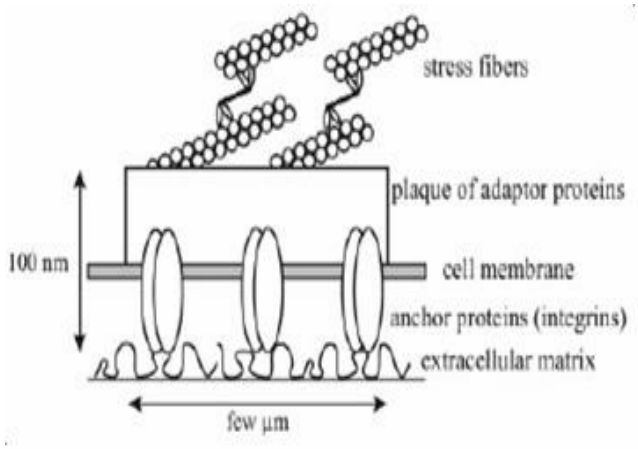

Fig. 1-3. Schematic representation of FAs
(Nicolas, Geiger et al. 2004)

FAs not only serve as mechanical anchors for the cell, but also relay signals between the cell and the ECM to modulate cellular responses. Integrins function as transducers for inside-out as well as outside-in signaling, and regulate cell motility through multiple signaling molecules. Phosphorylation and other signaling events are executed in the adhesion sites (Balaban, Schwarz et al. 2001; Li, Guan et al. 2005).

1.3. Previous Work on Measuring Forces Generated by Cells

The methods to measure the traction forces generated by cells can be categorized as the flexible substrate methods and the cantilever methods. The former involves the use of various forms of transparent flexible substrate, and the displacements of markers due to the deformation of the substrate are used to compute the traction forces. The latter uses deflection of cantilever to determine the traction forces.

1.3.1. Deformable Substrate Method

A. Wrinkling Silicone Substrate Method

Measurement of subcellular traction force was started more than 20 years ago by A.K. Harris et al. (Harris, Wild et al., 1980). Chick heart fibroblasts were cultured on thin silicone (Fig. 1-4) rubber film that had been polymerized with flame, and the contractile forces exerted by the cell caused the surface to wrinkle which could be visualized under the optical microscopy. Later, this approach was improved by replacing the flame with ultraviolet (UV) light (Burton and Taylor 1997), which provides optimal stiffness control of the substrate and a higher density of wrinkles for improved sensitivity and resolution (about 1 μm^2) (Fig. 1-5).

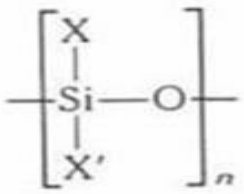

Fig. 1-4. Structure of silicone
(X, X': methyl or phenyl functional group)

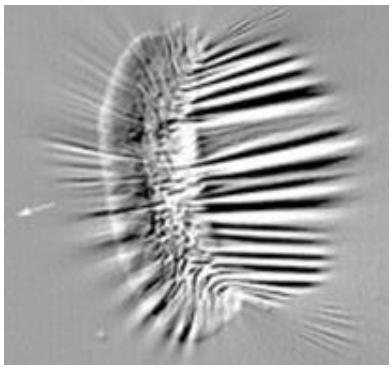

Fig. 1-5. Motile fish keratocyte
Arrow: direction of migration, (Image form K. Burton)

Contractile forces were estimated by multiplying the number of wrinkles and the stiffness of the substrate (Burton, Park et al. 1999). This is a simple and effective method to study traction forces at a qualitative level, but it has many limitations as a semi-quantitative method.

B. Non-Wrinkling Silicone Substrate Method

Improvement of the wrinkling silicone substrate method was achieved by attaching the silicone film to the inner wall of a chamber along the boundary, which prevented the surface from wrinkling but still allowed local deformation to occur, and tracking the movement of embedded particles that served as markers for substrate deformation (Oliver, Dembo et al. 1998) (Fig. 1-6).

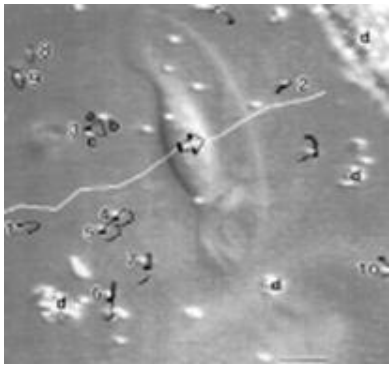

Fig. 1-6. Motile fish keratocyte
Arrow: direction of migration, Bar=10 μm, (Oliver, Dembo et al. 1998)

The non-wrinkling silicone substrate method enabled the application of physical equations for analysis, and thus has provided the first quantitative method for estimating the direction and magnitude of contractile forces. However, it has several disadvantages including non-physiological surface, low density of marker particles, non-elastic material properties, and complexity of preparation.

C. Micropatterned silicone (PDMS) substrate method

Micropatterned PDMS substrate method was the most improved form of non-wrinkling silicone substrate method (Fig. 1-7). It used silicon (Si) or gallium-arsenic (GaAs) mold to print the micropatterned PDMS elastomer substrate (Bershadsky, Balaban et al. 2003). [arsenite is a

compound which contains the arsenite ion ($H_2AsO_3^-$), arsenic is a adj. of element arsenide (As)]

This method has the advantages of improved elastic material properties and regular-graded micropatterning (2-μm space). Regular patterns enabled direct visualization of the contractile strain exerted by the cell and reduced the computational complexity when the force is calculated from the strain of the substrate. This method also provided the control of mechanical properties of the substrate by modulating the curing agent concentration, which could be useful to researchers who are interest in the effects of substrate stiffness on cellular functions.

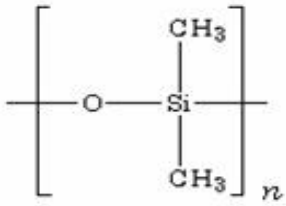

Fig. 1-7. Structure of polydimethylsiloxane (PDMS)

This method also has limitations. It requires complex photolithographic procedure to prepare the mold, which limits the availability of this method. Textured micropatterns could affect cell adhesion and migration through contact guidance (Weiss and Moscona 1958).

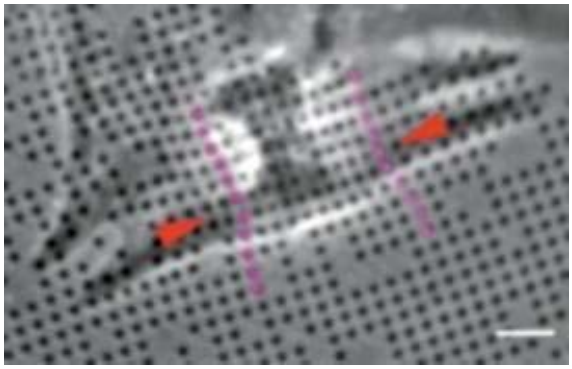

Fig.1-8. Stationary rat cardiac fibroblast
Arrows show the contraction by the cell, Bar=6 μm,
(Bershadsky, Balaban et al. 2003)

D. Polyacrylamide (PAA) method

Flexible polyacrylamide substrate was used to measure contractile forces of migrating cells (Pelham and Wang 1997). Stiffness of the polyacrylamide substrate could be controlled with different crosslinker (bis-acrylamide) concentrations (Fig. 1-9). Displacement of the fluorescent maker beads embedded in the deformable substrate was used to measure the traction force exerted by cells (Kaverina, Krylyshkina et al. 2000).

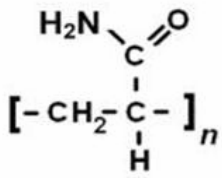

Fig. 1-9. Structure of polyacrylamide (PAA)

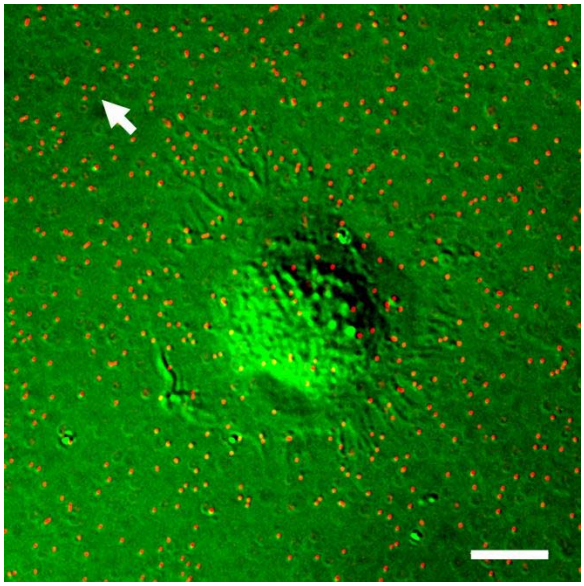

Fig.1-10. Motile bovine aortic endothelial cell
Arrow: Direction of migration, Red dots: TRITC Marker beads, (Bar=10 μm)

Polyacrylamide provided better mechanical and optical properties than silicone. Cells have low affinity to polyacrylamide so that the polyacrylamide deformable substrate is more appropriate to develop chemical approaches based on ECM coating methods. Moreover, the easy preparation procedure makes this method popular in cell mechanics study.

The problems of this method include the random distribution feature of the marker beads in the substrate, the need to remove the cell with trypsin in order to obtain a null-force reference state of the marker beads, and the requirement of complex computational procedures to quantify the traction forces from the measured bead displacements.

1.3.2. Cantilever Methods

A. Micromachined Cantilever Method

Micromachined cantilevers as force transducers on silicon wafers were devised as an alternative approach to the flat deformable substrate methods (Fig.1-11). The contractile forces were calculated from the deflection of the cantilevers (Galbraith and Sheetz 1998).

Because the mobile unit in micromachined devices (cantilever) was mechanically decoupled from its surrounding, the deflection of the cantilever resulted only from the local forces exerted on it (Fig. 1-12). The displacement was determined from the deflection with high precision. This feature circumvented complex computational analysis procedure due to the strain propagation effect which is a common difficulty in the deformable substrate methods. This cantilever method could also be applied to cells with high density.

In the cantilever method, however, only one-dimensional (1D) force can be measured along the line perpendicular to the pad, and the spatial resolution (100μm) of the pad is limited. Difficult construction steps of this device tend to limit the availability of this method. Furthermore, the non-uniform surface topology can affect the cell behavior.

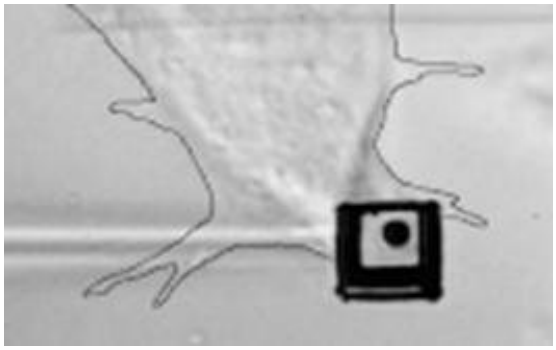

Fig. 1-11. Tail region of chick embryonic fibroblast moving across the detection pad
(Galbraith and Sheetz 1998)

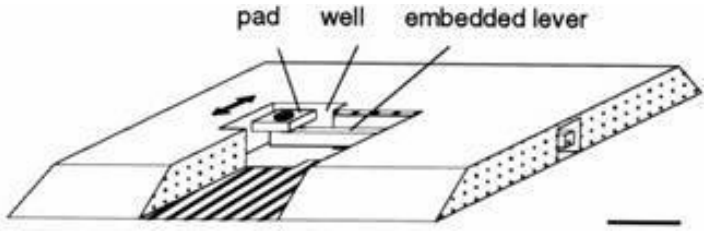

Fig.1-12. Micromachined device with cantilever
Bar = 10 μm (Galbraith and Sheetz 1998)

B. Pillar Method

Lithographic technique was used to mold the array of multiple cantilevers (or pillars) in a single substrate. The traction forces could be calculated from the deflection of vertical pillars in the PDMS elastomer (Figs. 1-13, 1-14).

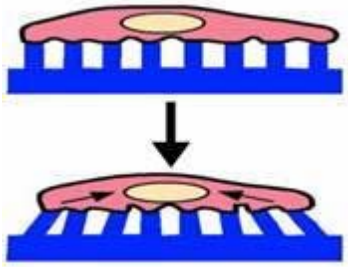

Fig.1-13 Cells exerting traction forces deflect the elastomeric posts
(Tan, Tien et al. 2003)

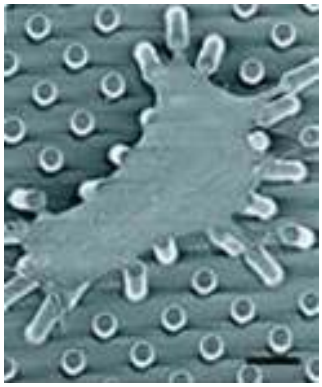

Fig.1-14 Smooth muscle cells (SMCs) attached to posts
Bar: 10 μm (Tan, Tien et al. 2003)

Since each pillar moves independently to its neighbors, its deflection directly reports the direction and magnitude of the local cell-generated forces, and this allows a simple calculation of the traction forces as micromachined cantilever method. But this method is limited in spatial resolution (pod space ~10μm), and the cell can be affected by the surface topology by contact guidance (Weiss and Moscona 1958). [Do you think is it necessary to describe the contact guidance or just the reference is enough?] Small deformation of the pillar must be assumed to calculate the traction force. Moreover, it is difficult to construct the substrate because of the complex photolithography procedure.

1.3.3. Previous Findings on Traction Force Measurements

A. Traction Force and Adherent Cells

The methods mentioned above have been applied to research studies on contractile forces exerted by live cells. For migrating fibroblasts, micromachined cantilever method has shown strong traction forces localized at the anterior and posterior regions pointing toward the center of the cell (Galbraith and Sheetz 1998; Paszek, Zahir et al. 2005). These results are consistent with the observations using wrinkling substrate (Harris, Wild et al. 1980). Studies with the

polyacrylamide method and using myosin inhibitors have shown that the traction force is generated by acto-myosin contractile machineries in the cell. Two dimensional (2D) spatial pattern studies have shown that the front region serves as the 'engine' that tows the cell body and tail, while the rear region works as a passive anchor (Pelham and Wang 1999; Munevar, Wang et al. 2001).

B. Traction Force and Focal adhesions

Recent traction force studies combined with GFP imaging methods have demonstrated that nascent FAs or focal complexes are responsible for the generation of strong propulsive force in the frontal region of migrating fibroblasts (Kaverina, Krylyshkina et al. 2000). The magnitude of traction forces decreases as FAs become mature, and the FAs maintain a constant stress after maturation (Bershadsky, Balaban et al. 2003). These studies have shown that the sizes of the individual FAs determined by fluorescence microscopy correlate loosely with the measured local forces, except for the smaller nascent focal adhesions (<1μm). These results suggest that different FAs have different mechanical functions depending on their age and the state of cell motility (Chen, Tan et al. 2004). Furthermore, the maturation of FAs appears to require the application of mechanical stress to the adhesions (Ridley and Hall 1992; Balaban, Schwarz et al. 2001). Previous studies have shown that the application of external forces on human and mouse fibroblasts cause FAs to increase in size, to stabilize, and to strengthen their coupling to the cell through the actin cytoskeleton (Riveline, Zamir et al. 2001).

1.3.4. What Is Missing?

Traction force microscopy studies were mainly confined to 2D ECM-coated surfaces. Both the deformable substrate methods and the cantilever methods consider only the traction force

tangential to the substrate on which the cell is attached, with the assumption that the traction force normal to the substrate is negligible. However, the following considerations indicate that it would be more appropriate to consider forces with three-dimensional (3D) components, i.e., including the normal component as well as tangential component, for studies of adherent cells and their FA dynamics.

(1) The cell itself has 3D shape with many structural components in it.
(2) In the natural in vivo situation, the cell is located in a 3D environment.
(3) There is evidence that cells can sense and respond to the 3D geometry (Vogel and Sheetz 2006).

1.4. Aims of the Present Study

The aims of the present study are as follows

(1) To develop a method to measure the 3D traction forces generated by the bovine aortic endothelial cell (BAEC).
(2) To develop a method to measure the 3D traction forces on each FA in the BAEC.
(3) To elucidate the existence and the characteristics of 3D traction forces, including the normal component, of migrating BAEC.
(4) To elucidate the interrelations between the 3D traction forces, including the normal component, and the FA dynamics of migrating BAEC.

II. MATERIALS AND METHODS

2.1. Cell Culture

Bovine aortic endothelial cells (BAECs) were isolated from the bovine aorta with collagenase (Li, Chen et al. 1999). Cell culture reagents were purchased from Invitrogen (GIBCO/Invitrogen Corp., Carlsbad, CA) unless otherwise mentioned. The cells were cultured in a 10-cm Petri dish containing Dulbecco's modified Eagle's medium supplemented with 10% fetal bovine serum (FBS), 1% sodium pyruvate, 1% L-glutamine, and 1% penicillin-streptomycin. Cell culture was maintained in a humidified 5% CO_2 / 95% air incubator at 37°C. Experiments were conducted with cells prior to passage 15.

2.2. DNA Transfection

Green fluorescent protein (GFP) transfection technique was used to visualize the FAs of live BAECs. GFP-paxillin and GFP-focal adhesion kinase (GFP-FAK) were transfected into BAECs with FuGene 6 (F. Hoffmann-La Roche Ltd., Basel, Switzerland), and the cells were used after 2 days. GFP-paxillin plasmid was provided by Dr. Donna J. Webb (Department of Cell Biology, UVA School of Medicine, Charlottesville, Virginia), and GFP-FAK plasmid by Dr. Jun-Lin Guan (Department of Molecular Medicine, Cornell University, Ithaca, New York) as gifts.

2.3. Preparation of Polyacrylamide Deformable Substrate

Polyacrylamide deformable substrate was prepared as described below, based on the method developed by Yuli Wang et al. (Pelham and Wang 1997; Beningo, Lo et al. 2002).

2.3.1. Glass Coverslip Activation

The glass coverslip (No. 1, 35 × 60 mm, Fisher Scientific International, Pittsburgh, PA) was washed with 70% ethanol to clean the surface, and activated with inner flame using a Bunsen burner to make the glass surface hydrophilic. The surface was smeared with 0.1 M sodium hydroxide (NaOH, Merck & Co., Inc., Whitehouse Station, NJ) and air dried, and then siliconized with 3-aminopropyl triethoxy silane (Sigma-Aldrich Co., St. Louis, MO) followed by activation with 0.5% glutaraldehyde (Sigma), which ensured the attachment between the glass coverslip and the polyacrylamide substrate (Aplin and Hughes 1981). Covalent bonds between glass surface and polyacrylamide were formed after the procedure (Fig. 2-1).

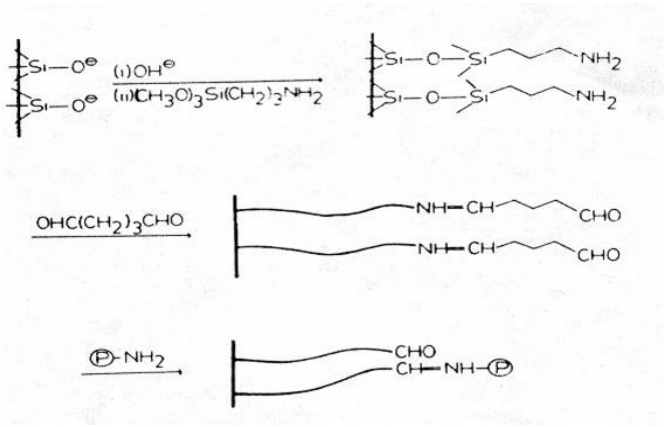

Fig. 2-1. Activation of glass coverslip to couple its surface to the polyacrylamide (Aplin and Hughes 1981)

The activated glass slides were stored in a desiccator (Bel-Art Products, Inc., Pequannock, NJ) at room temperature, and have been used within one month (Fig. 2-2).

Fig. 2-2. Desiccator attached to a vacuum

2.3.2. Polymerization

The monomer solution was prepared with acrylamide (40% w/v, Bio-Rad Laboratories, Inc, Hercules, CA), N,N'-methylene bis-acrylamide (bis-acrylamide) (2% w/v, Bio-Rad), 4-(2-hydroxyethyl)-1-piperazineethanesulfonic acid (HEPES) buffer (1 M, pH 8.5, EMD Chemicals Inc., Gibbstown, NJ), 0.2-μm diameter red (580/605) fluorescent polystyrene beads (FluoSpheres, Molecular Probes/ Invitrogen Corp., Carlsbad, CA), and distilled water. The final concentrations were 5% for acrylamide (monomer), and 0.1 to 0.3% for bis-acrylamide. The stiffness of the polyacrylamide was controlled by changing the concentration of the bis-acrylamide (crosslinker). Polymerization was started when 0.06% ammonium persulfate (APS, SIGMA) and 0.4% N,N,N',N'-tetramethylene diamine (TEMED, Invitrogen) were added to the monomer solution. APS is an initiator and TEMED is a catalyst for the polymerization. The monomer solution was allowed to polymerize for 40 min at room temperature (Fig. 2-3).

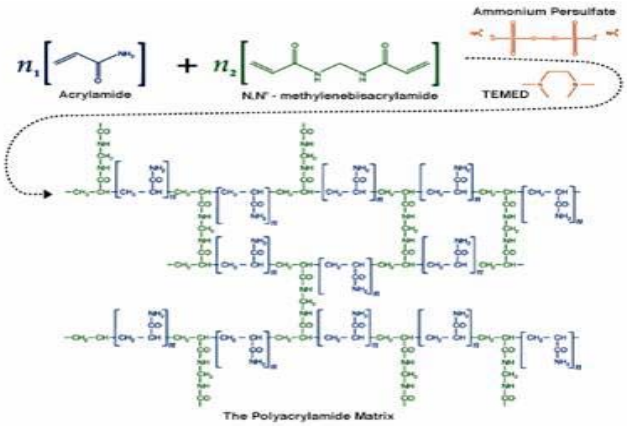

Fig. 2-3. Polymerization of the acrylamide
(http://nationaldiagnostics.com/article_info.php/articles_id/6)

.

2.3.3. Filtration and Sonication of the Beads

The fluorescent beads with 0.2-μm diameter, which have a large surface-to-volume ratio, aggregated easily although their surface had been modified with carboxylate group to reduce the

aggregation. Therefore, the fluorescent beads were sonicated for 5 min in the ultrasonic sonicator (BANSONIC®, BRANSON ULTRASONICS Corp., Danbury, CT) to disperse the aggregates. The bead suspension was syringe driven through 0.22-μm filters (MILLEX, Millipore Corp., Billerica, MA) to remove the aggregated beads. Typically, about 30% of the beads were removed after this filtration procedure.

2.3.4. Extracellular Matrix Coating

The surface of the polyacrylamide was coated with the ECM protein bovine fibronectin (FN, SIGMA) to allow the adhesion of BAECs. N-Sulfosuccinimidyl-6-[4'-azido-2'-nitrophenylamino] hexanoate (Sulfo-SANPAH, Pierce Biotechnology, Rockford, IL), which has two different functional groups that can couple FN and polyacrylamide, was used to allow the FN to be attached on the polyacrylamide substrate. A phenylazide group in the Sulfo-SANPAH reacts with polyacrylamide upon ultraviolet (UV) activation, and the sulfosuccinimidyl group reacts with the primary amines of FN (Fig. 2-4). FN was diluted in phosphate buffered saline (PBS), and 200 μl of 4 μg/cm^2 solution was spread on the polyacrylamide substrate which had been activated with Sulfo-SANPAH solution in the previous step. The FN-coated polyacrylamide substrates were incubated overnight at 4°C.

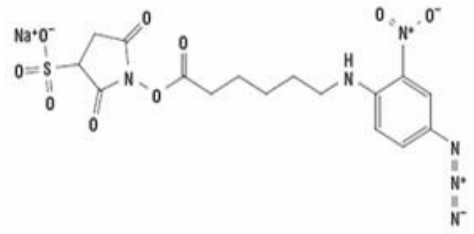

Fig. 2-4. Sulfo-SANPAH with sulfosuccinimidyl (left) and phenylazide (right) groups

2.4. Characterization of Polyacrylamide

2.4.1. Calculation of Bead Concentration in Acrylamide Solution

The bead concentration (number per volume) in the monomer solution could be calculated from the following equation.

$$Concentration(\#/mL) = \frac{6C \times 10^{12}}{\rho \times \pi \times \phi^3}$$

Where C: Concentration of beads in g/mL,
(e.g. 0.01 g/mL for 1% suspension)
ϕ: Diameter of bead = 0.2 μm
ρ: Density of bead = 1.05 g/mL (for polystyrene)

2.4.2. Determination of Bead Concentration in Polyacrylamide Gel

The concentration of the syringe-filtered beads before the polymerization [OK??] was optically determined with a spectrophotometer (U-20900, Hitachi Ltd., Santa Clara, CA). Although spectrophotometer is typically used to determine the concentration of a solution, it was possible to measure the concentration of the fluorescent beads in the solid polyacrylamide gel. Linearity of the standard curve of optical density (absorbance) vs. bead concentration shows that the Beer-Lambert law can be applied to this system (Odian 2004).

2.4.3. Determination of the Young's Modulus

To determine the elastic property of the polyacrylamide, Young's modulus was determined with a compressive test device (V500cs, Biosyntech Inc., Laval, Québec, Canada) (Fig.2-5A). 5% polyacrylamide specimens (Diameter = 6 mm, Thickness = 3 mm) with different concentrations of bis-acrylamide crosslinker were prepared using the same protocol as that for polyacrylamide deformable substrates (Section 2.3.2). During the experiment, the polyacrylamide specimens were kept in cell culture medium to prevent drying (Fig. 2-5B). Stresses were measured with the application of compressive strains from 0 to 25% to the polyacrylamide specimens (Fig. 2-6).

Young's modulus was calculated from the stress-strain curve.

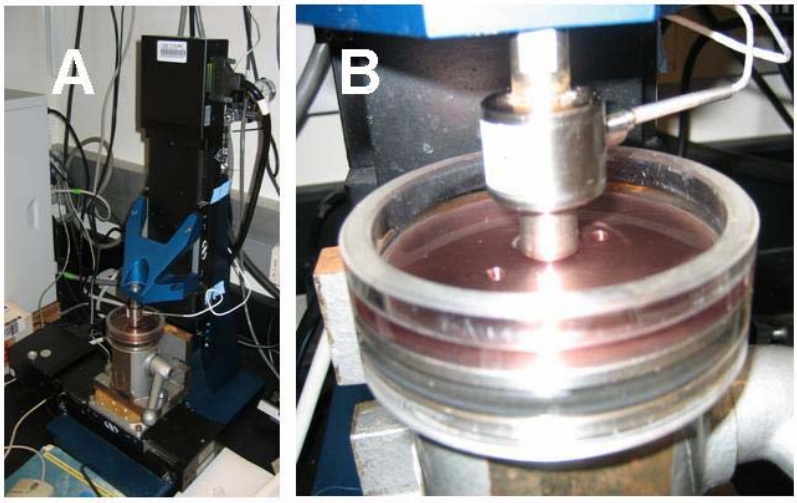

Fig. 2-5. Compressive test device to measure Young's modulus
A. Whole view of the compressive test device
B. Compression head and chamber containing the sample and the growth media

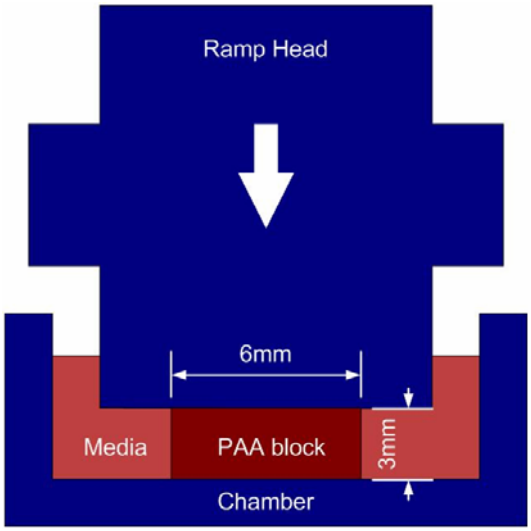

Fig. 2-6. Schematic of the compressive test device
Arrow: Direction of ramp head movement in experiment

2.4.4. Assessment of the Viscoelasticity of the Polyacrylamide Specimen with a Compressive Relaxation Device

A compressive relaxation device (Fig.2-7) was used to determine whether the polyacrylamide specimen has a significant viscous component. 5% polyacrylamide specimens with 0.3% bis-

acrylamide crosslinker (Diameter = 6 mm, Thickness = 3 mm) were prepared with the same protocol as that of polyacrylamide deformable substrate (Section 2.3.2). During the experiment, the polyacrylamide specimens were kept in a growth medium to prevent drying. Stress was measured while strain (from 0 to 20%) with 1 hour relaxation time was applied to the specimen.

Fig. 2-7. Relaxation test device

2.4.5. Assessment of Biocompatibility

0.2% trypan blue (Invitrogen) in PBS buffer solution was added to the BAECs which had been cultured overnight on the polyacrylamide deformable substrate (Fig. 2-8), and incubated for 10 min. The trypan blue solution was then washed with PBS one time, and the BAECs were observed under the microscope. Trypan blue traverses the membrane in non-viable cells, which thus show a distinctive blue color. Trypan blue is not absorbed in viable cells because normal cell membrane does not allow its passage.

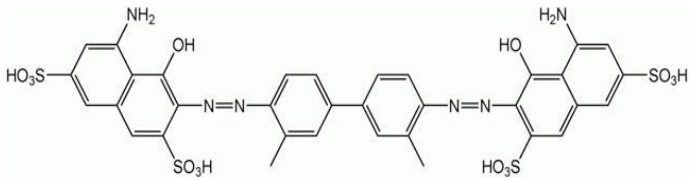

Fig. 2-8. Structure of trypan blue

2.5. Traction Force Microscopy

2.5.1. UV sterilization and Cell Seeding

FN-coated polyacrylamide substrates were exposed to the UV light (SPECTROLINE, Spectronics Corp., Westbury, NY) for 10 min to minimize microbial contamination. This "quasi-sterilization", combined with the use of antibiotics (penicillin-streptomycin), kept microbial contamination under control for at least 2-3 days (Beningo, Lo et al. 2002). BAECs were spread on the substrate after it had been equilibrated in the cell culture media for 1 hr. The tubings were sterilized in an autoclave (SG-116, AMSCO Scientific, Apex, NC) for 30 min at 121°C. Cells were allowed to be attached on the FN-coated polyacrylamide substrate overnight.

2.5.2. Cell Chamber

To keep the live BAECs during the traction force microscopy experiment, the chamber with the design described below was used (Fig. 2-9). A rectangular flow channel (1000 μm in height, 2.3 cm in width, and 5 cm in length) was formed by sandwiching a silicone gasket between the 35×60 mm glass slide with the polyacrylamide substrate and a glass plate attached onto the aluminum housing (Fig. 2-9A). The entire assembly was tightened with screws between four aluminum parts (dashed parts in Fig. 2-9B) and the aluminum plate, which has a central opening to allow the visualization of the channel with a microscope.

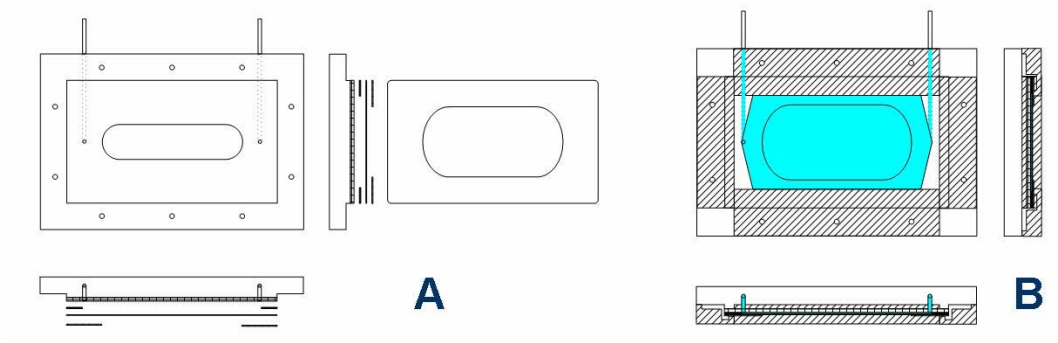

Fig. 2-9. Schematic diagram of the chamber design
A: Disassembled form
B: Assembled form, Blue: Flow channel formed

2.5.3. Microscopy and Image Acquisition

A spinning disk confocal microscope (IX-81, Olympus, Olympus America Inc., Center Valley, PA) with a 60X objective lens (UIS Plan-Apo, N.A. 1.40, Olympus) was used to determine the deformation of the substrate in 3D by tracking the motions of the imbedded fluorescence beads (Fig. 2-10A).

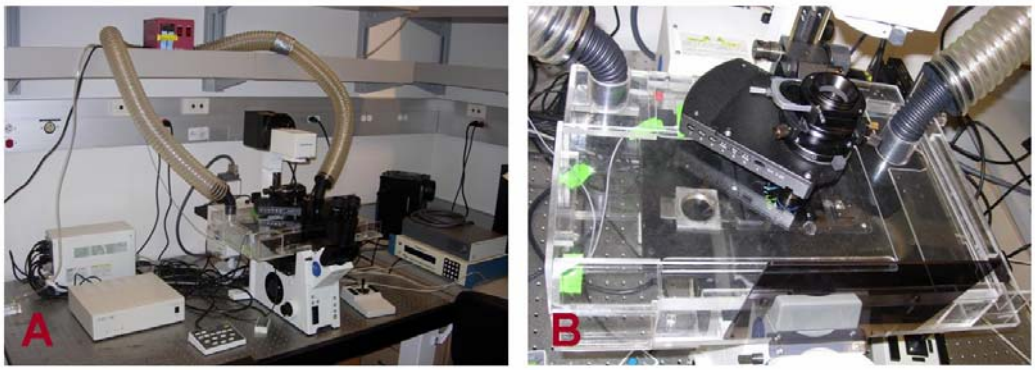

Fig. 2-10. Inverted Spinning Disk Confocal Microscope system
A: Whole view, B: Temperature control box

Differential interference contrast (DIC) microscopy was used to acquire the BAECs images, and fluorescent microscopy was used to acquire the images of the red fluorescent (580/605) beads and GFP (490/509). Images were acquired with charge-coupled device (CCD) camera (ORCA-II-ER,

Hammamatsu Photonics K.K., Hamamatsu, Shizuoka, Japan). The polyacrylamide deformable substrate was optically sectioned with 0.2-μm thickness to obtain the 3D images of the fluorescent beads. The image acquisition for one experiment was completed within 3 hours. The chamber was kept at 37°C with a temperature control system (Fig. 2-10).

2.6. Image Enhancement

Several computational image restoration techniques, including background subtraction, 2D-deconvolution, 3D-deconvolution, and median filtering were used to enhance the images acquired from the experiments. Meta-Morph 6.3 (Molecular Devices, Corp., Downingtown, PA) was used for the image enhancing procedures, including background subtraction, 2D-deconvolution (no-neighbor scheme), and median filtering. AutoQuant 9 (Media Cybernetics Inc., Bethesda, MD) was used for the 3D-deconvolution procedure (no-neighbor scheme).

2.7. Measurement of 3D Displacement of Marker Beads

2.7.1. Measurement of 3D Coordinates

Image processing programs were encoded with MATLAB (MATLAB 7.0, The MathWorks Inc., Novi, MI) to obtain 3D coordinates of TRITC fluorescent beads. The original images acquired with the CCD camera were the 16-bit grayscale type data. These grayscale images were converted into 1-bit binary images to determine the properties of the specified image regions, such as the center of mass and the volume of the beads (Fig. 2-11). This binarization technique is known as thresholding which is the method of image segmentation. The threshold is a value used to define the "object" vs. the "background". Individual pixels in a grayscale image are marked as “object” pixels if their intensity value is greater than the threshold value and as

"background" pixels otherwise (assuming an object is brighter than the background). An object pixel is given a value of "1", while a background pixel is given a value of "0" (Fig. 2-11).

If $I \geq \theta$, I = object = 1 (white)

Otherwise, I = background = 0 (black)

In our image processing program, the objects are the beads. After the binarization, the center of mass (3D coordinates) and volume of the beads can be calculated. The volume of the bead was used as a characteristic of each bead, and this was exploited to improve the accuracy of the particle tracking algorithm (PTA) to track the movement of the beads. Tracking beads with PTA at different time points will be discussed further (Section 2.7.2).

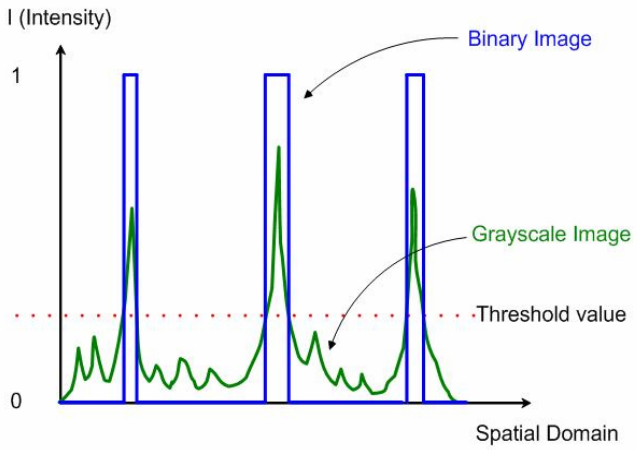

Fig. 2-11. Schematic principle of binarization (thresholding)

2.7.2. Particle Tracking Algorithm

Three particle tracking algorithm (PTA) programs were encoded with MATLAB. The purpose of PTA was to track beads at different time points, in order to calculate the displacements from the measured coordinate changes of the beads.

In brief, the nearest-neighbor (NN) algorithm uses only one feature (distance), whereas the five-neighbors and nearest-volume (5NV) algorithm uses two features (distance and volume), and the five-neighbors and nearest-volume with angle-constraint (5NVA) algorithm uses three

features (distance, volume and movement trend). The concepts for these three PTAs are detailed next.

Testing of these three algorithms with shifted 3D image stacks showed that 5NVA had a better performance than 5NV, and both had much better performance than NN.

A. Nearest-Neighbor (NN) Algorithm

NN algorithm is the simplest PTA for tracking the movement of the beads, applying only the distance condition (nearest neighbor is elected among many candidates) for the particle tracking (Fig. 2-12<1>). After the bead has been tracked, displacement vector can be calculated from the centroids at the two time points (Fig. 2-12 <2>). When the movement of the bead is small, NN gives a good performance.

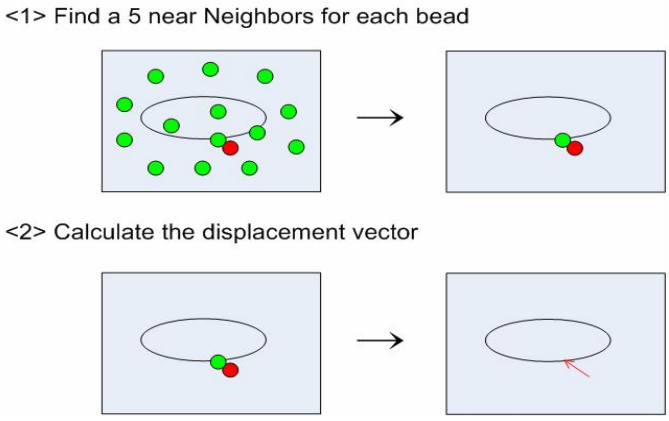

Fig. 2-12. Schematic principle of the NN algorithm
Red bead: Data point at time = t_0
Green bead: Candidates of the match at time = t_1
Red arrow: Displacement vector determined, Ellipse: Cell

B. Five-Neighbors and Nearest-Volume (5NV) Algorithm

5NV algorithm is an improved algorithm from NN in that it uses the volume of the particle in addition to the distance, to track the beads. 5NV applies the distance condition first (5 near neighbors are chosen as candidates) (Fig. 2-13<1>), and then the volume condition (the bead with

the closest volume is elected among the 5 candidates), for the particle tracking (Fig. 2-13 <2>). After the bead has been tracked, the displacement vector can be calculated from the centroids at two time points (Fig. 2-13 <3>). The performance of 5NV algorithm was far better than that of NN algorithm.

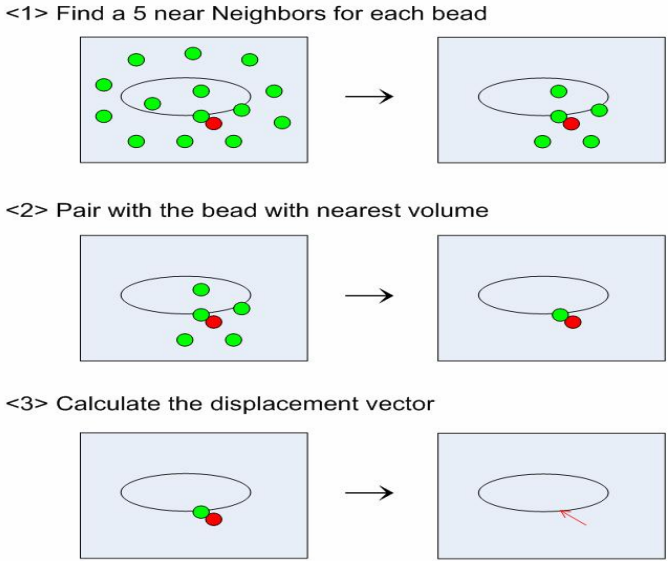

Fig. 2-13. Schematic principle of 5NV algorithm
Red bead: Data point at time = t_0
Green bead: Candidates of the match at time = t_1
Red arrow: Displacement vector determined, Ellipse: Cell

C. Five-Neighbors and Nearest-Volume with Angle-Constraint (5NVA) Algorithm

5NVA algorithm is a more advanced PTA than NN and 5NV algorithms since 5NVA algorithm uses not only the distance and volume of the particle, but also the trend of particle movement. 5NVA algorithm applies distance condition first and volume condition next as the 5NV algorithm (Fig. 2-14 <1-3>), but 5NVA algorithm finally applies the condition of bead movement trend condition (angle constraint condition) (Fig. 2-14 <4>). When the movement of the bead is smaller than the criterion (0.216 μm), application of particle movement trend condition is skipped. After the bead has been tracked, displacement vector can be calculated from the centroids at two time points (Fig. 2-14 <5>).

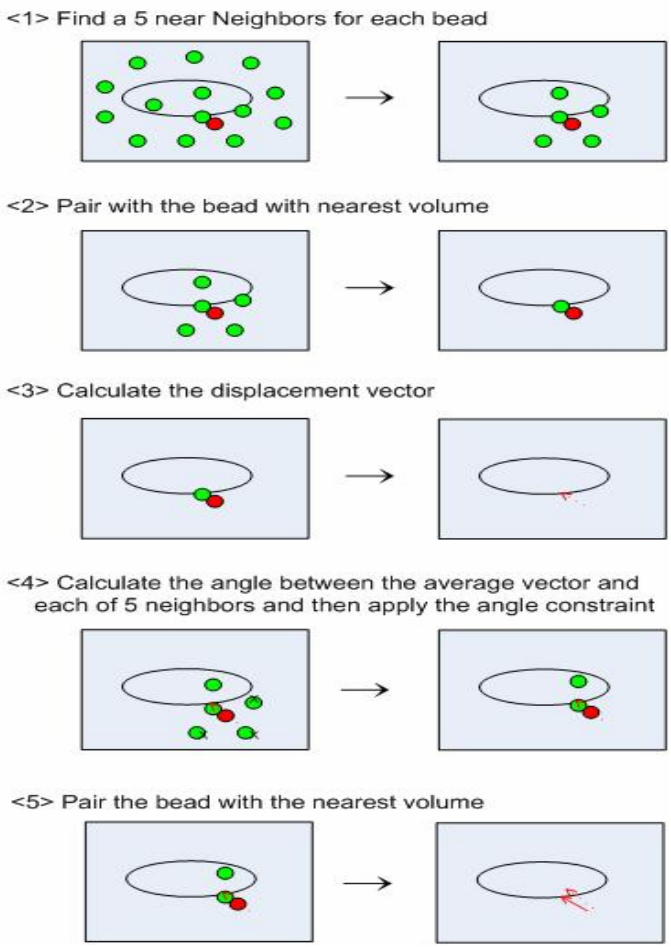

Fig. 2-14. Schematic principle of 5NVA algorithm
Red bead: Data point at a reference time point t_0
Green beads: Candidates of the pair for the red bead at a time point t
Red dotted arrow: Preliminary displacement vector
Red solid arrow: Displacement vector determined, Ellipse: Cell

2.7.3 Resolution of Displacement Measurement

Resolution, which is the limit of bead displacement that can be measured, was evaluated with the beads located at the bottom (from the glass coverslip surface to 1 μm above this surface) (Fig 2-15). Ideally, beads should show zero movement in this block because the glass coverslip prohibits the deformation of the polyacrylamide substrate. The measured displacement histogram shows normal distribution around a mean value 0; the dispersion around 0 can be attributed to the errors originated from the experiment (image acquisition, CCD digitization) and

image processing procedures (image enhancement, segmentation) (Fig. 2-16).

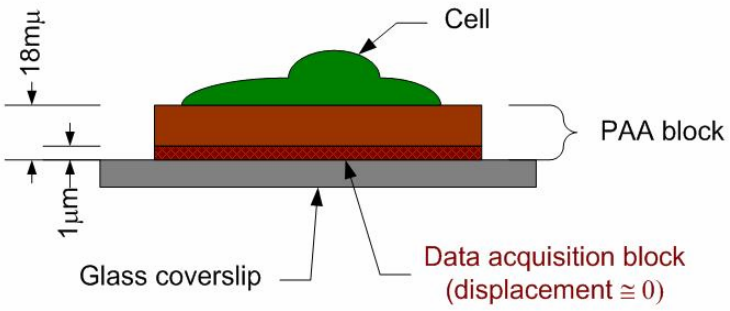

Fig. 2-15. Data acquisition block to evaluate the resolution

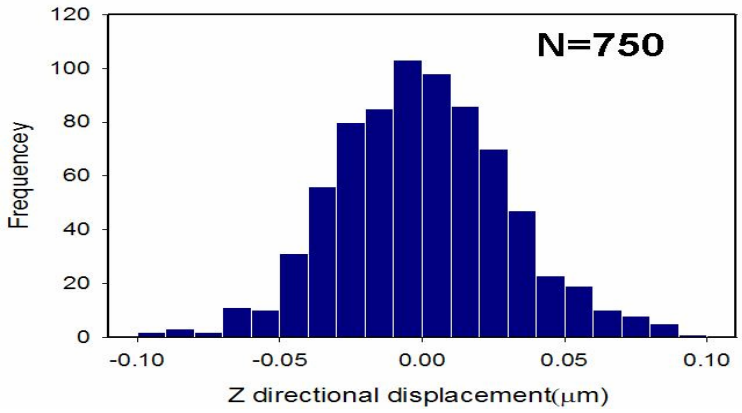

Fig. 2-16. Frequency distribution of bead displacement at the substrate bottom
N: Number of beads at the substrate bottom (data acquisition block in Fig. 2-15)

The standard deviation of displacements in each coordinate is used as a measure of resolution in each coordinate (Fig. 2-17). Thus, the resolution as a lower limit of the accuracy of the displacement measurement of our method can be defined from the magnitude of the 3D standard deviation vector σ.

$$|\sigma| = \sqrt{\sigma_x^{\,2} + \sigma_y^{\,2} + \sigma_z^{\,2}}$$

Where $\sigma = [\sigma_x, \sigma_y, \sigma_z]$
σ_x = Standard deviation of the displacement in X direction
σ_y = Standard deviation of the displacement in Y direction
σ_z = Standard deviation of the displacement in Z direction

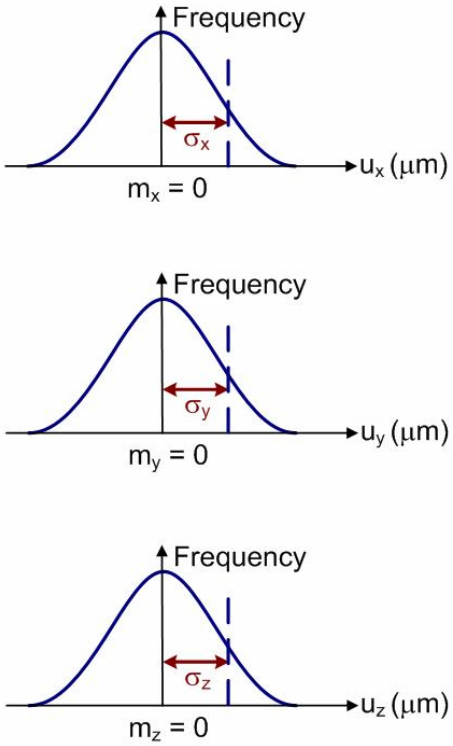

Fig. 2-17. Schematic of the resolution definition of bead displacement measurement
m_x, m_y, m_z = mean of the displacement in each coordinate
σ_x, σ_y, σ_z = standard deviation of the displacement in each coordinate

2.8. Calculation of 3D Traction Force

2.8.1. Finite Element Method (FEM)

The finite element method (FEM) was used to calculate the 3D traction force from the 3D displacement. FEM is a general technique for constructing a computational solution for boundary value problems (BVPs). FEM involves dividing the domain of the solution into a finite number of sub-domains (the finite elements), and using variation concepts to construct an approximation of the solution over the collection of finite elements. It has been used with success in solving a wide range of problems in virtually all areas of engineering and mathematical physics (Becker, Carey et al. 1981).

2.8.2. Domains of the Boundary Value Problem

The domain used for the stress analysis is shown in Fig. 2-18. Ends of the domain in x direction are at x=0 and x=X_L, while ends of the domain in y direction are at y=0 and y=Y_L. Top of the polyacrylamide substrate on which the cell is attached is at Z=0 while bottom of the substrate under which the glass coverslip is attached is at Z=Z_L.

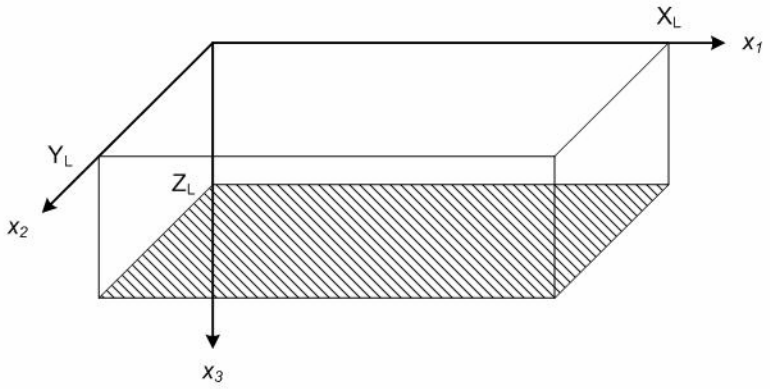

Fig. 2-18. A rectangular parallelepiped domain used for stress analysis
(x_1, x_2, x_3) = (x, y, z): Cartesian coordinates
z = 0: Top of the substrate, z = Z_L: Bottom of substrate

2.8.3. Assumptions

(1) The polyacrylamide substrate is an elastic material.

There are no viscous properties.

(2) The polyacrylamide substrate has isotropic elastic material properties.

The polyacrylamide follows Hooke's law

$E_1 = E_2 = E_3 = E$

$\nu_1 = \nu_2 = \nu_3 = \nu$

Where E_i: Young's Modulus in each direction (i = 1, 2, 3)
ν_i: Poisson's ratios in each direction (i = 1, 2, 3)

2.8.4. Governing equations

A. The strain-displacement equation

$$\varepsilon_{ij} = \frac{1}{2}\left(\frac{\partial u_i}{\partial x_j} + \frac{\partial u_j}{\partial x_i} \right)$$

Where ε_{ij}: Strain tensor (i, j = 1, 2, 3)
u_i: Displacement vector
x_i: Cartesian coordinates (i=1,2,3)

B. The elastic stress-strain law (Hooke's Law)

$$\varepsilon_{ij} = \frac{1}{E}\left\{ (1+\nu)\sigma_{ij} - \nu\delta_{ij}\delta_{kk} \right\}$$

Where σ_{ij}: Stress tensor
E: Young's modulus
ν: Poisson's ratio
δ_{ij}: Kroneker delta

C. The equation of static equilibrium for stresses

$$\frac{\partial \sigma_{ij}}{\partial x_i} = 0$$

D. The boundary conditions on displacement and stress

$$u_i = u_i^* \quad at\ x_3 = 0$$

$$u_i = 0 \quad at\ x_3 = Z_L$$

Where u_i^*: Measured displacement at the top plane

2.8.5. Materials Properties

The value of Young's modulus measured in the previously mentioned experiment (Section 2.4.3) was used. Since the traction force is not sensitive to the Poisson's ratio (ν), the value of 0.3 was used as measured in a previous study (Li, Hu et al. 1993).

2.8.6. Processing Parameters

ABAQUS 6.3 (ABAQUS, Inc, Providence, RI), a commercial software package for finite

element analysis, was used to solve the 3D BVP. It has been widely used in the automotive, aerospace, and industrial products industries. Hexahedron reduced integration element (C3D8R), which has 8 nodes at the corner and one integration points in the middle, was used (Fig. 2-19). 2-μm fixed mesh grids were used as ΔX and ΔY, and adaptive mesh grids were used for ΔZ. The ratio between ΔZ and ΔX (ΔZ /ΔX) was maintained less than 4. ABAUS/Standard implicit solver was used to solve BVP defined above. The force equilibrium inside of the BVP domain was also verified using the results of calculation.

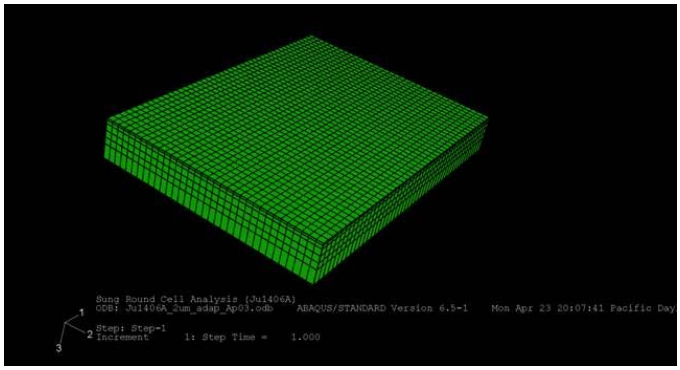

Fig. 2-19. Mesh generated for the FA analysis
(1, 2, 3 = x, y, z = Cartesian coordinates)

2.9. Quantification of Focal Adhesions

Focal adhesion characteristics, including coordinates, area, length, and aspect ratio, were measured using the image morphometry function in Meta-Morph 6.3 and the image processing program coded with MATLAB. Before the quantification, GFP-paxillin and GFP-FAK images were enhanced using 2D deconvolution (no neighbor scheme) and background subtraction with Meta-Morph 6.3, as mentioned above (Section 2.6).

2.10. Summary of Methods for Traction Force Measurement

The whole procedure of the 3D traction force microscopy method and the flow of the

information in each step are summarized with a flow chart (Fig. 20). Dark blue blocks show the sequence of transformation of the information, and the light blue blocks represent the operational procedures which are needed to convert the form of the information.

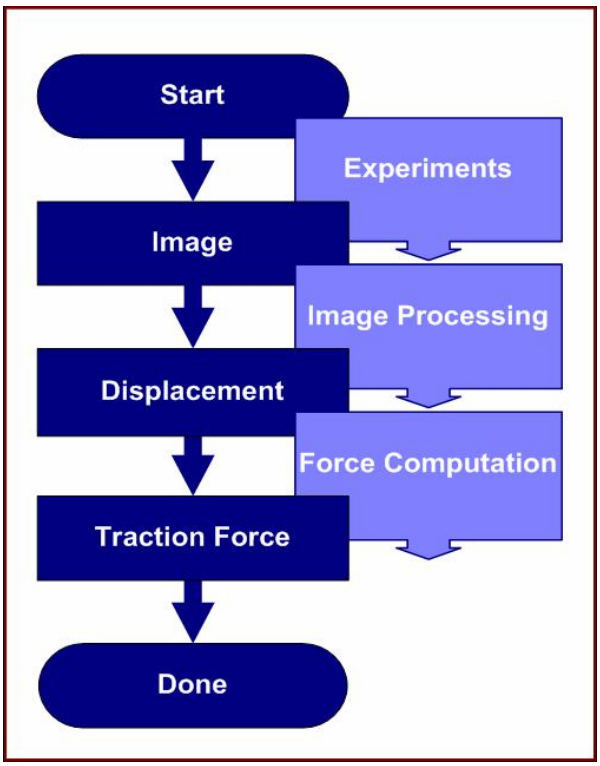

Fig. 2-20. Flow chart of the traction force microscopy
Dark blue: Sequence of the information
Light blue: Sequence of operation

III. RESULTS

3.1. Characterization of Polyacrylamide Deformable Substrate

3.1.1. Confirmation of Elasticity

Relaxation test showed no significant time-dependent change and verified the elasticity of the polyacrylamide deformable substrate (Fig. 3-1). Stress relaxation was about 1%, and it is not significant after the T-test (P value = 0.9860, N=3)

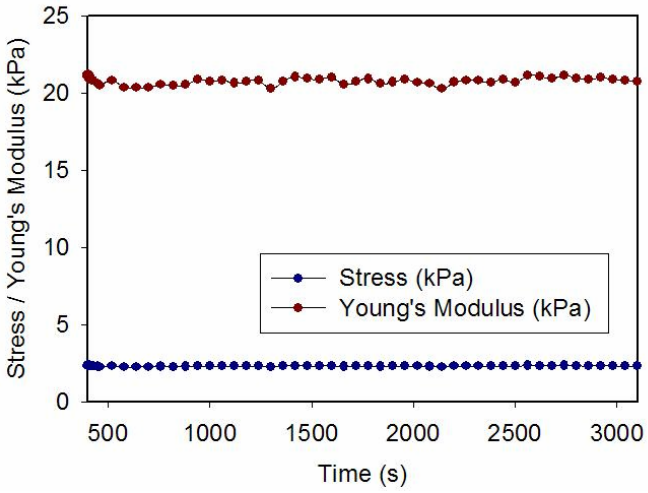

Fig. 3-1. Relaxation test verifying elasticity of the polyacrylamide
0.5% acrylamide, 0.3% bis-acrylamide, applied strain =10%

3.1.2. Elastic Material Properties

Stress-strain curve of the polyacrylamide can be fitted with a linear regression curve of y = 7.614x - 0.121, with a high R^2 value of 0.988 (Fig. 3-2). There are many numbers of data so that the scatter plot looks like a line

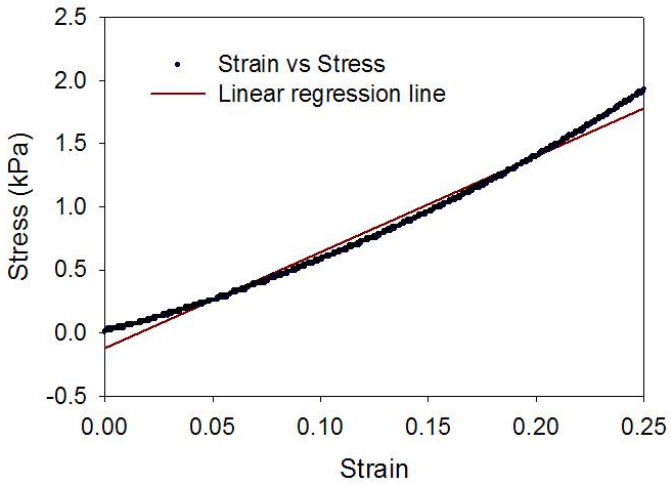

Fig. 3-2. Stress-strain curve showing linear regression relationship
0.5% acrylamide, 0.3% bis-acrylamide
Blue: Scatter plot of strain vs. stress, Red: Linear regression line

The measured Young's moduli at various percentages of bis-acrylamide are shown in Table 3-1. The strain from 0 to 25 % was applied in this test, because it has been reported that the maximum strain applied to the polyacrylamide deformable substrate by the migrating cell is about 15~25% (Lo, Wang et al. 2000)

Table 3-1. Measured Young's moduli and standard deviation

Bis (%)	E (kPa)	SD (kPa)
0.05	2.64	0.30
0.10	3.78	0.36
0.30	7.59	0.30
0.60	8.91	0.71

0.5% acrylamide, applied strain: 0~25%, N=4 for each Bis
Bis: Concentration (%) of the bis-acrylamide crosslinker.
E: Young's Modulus, SD: Standard Deviation

Young's modulus becomes higher as the crosslinker concentration increases. Moreover, Young's modulus is linearly related (proportional) to the concentration of the crosslinker up to 0.3% (Fig. 3-3). These results are consistent with the previous study using atomic force microscopy (AFM) and tensile test (Fig. 3-4) (Engler, Bacakova et al. 2004).

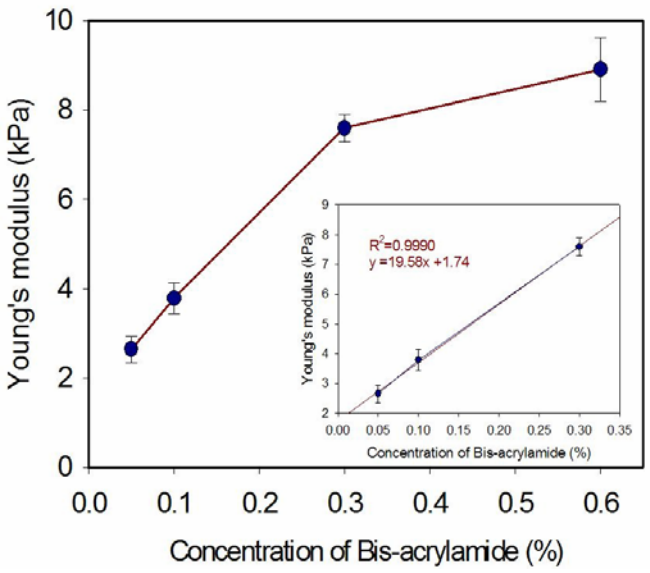

Fig. 3-3. Polyacrylamide gel elasticity vs. bis-acrylamide crosslinker concentration
By compressive test, Bis = 0.05 ~ 0.6 %
Inset: Data for Bis = 0.05 ~ 0.3 %, with result of linear regression analysis

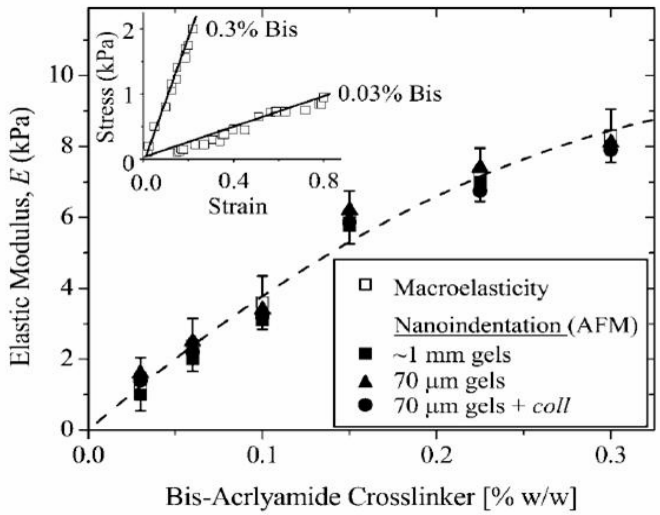

Fig. 3-4. Polyacrylamide gel elasticity vs. bis-acrylamide crosslinker concentration
By tensile test and AFM test, Bis=0.03 ~ 0.3%.
(Engler, Bacakova et al. 2004)

3.1.3. Biocompatibility

No BAECs were stained by the trypan blue after overnight incubation on the polyacrylamide substrate, indicating that the BAECs are viable on the polyacrylamide deformable substrate (Fig.

3-5).

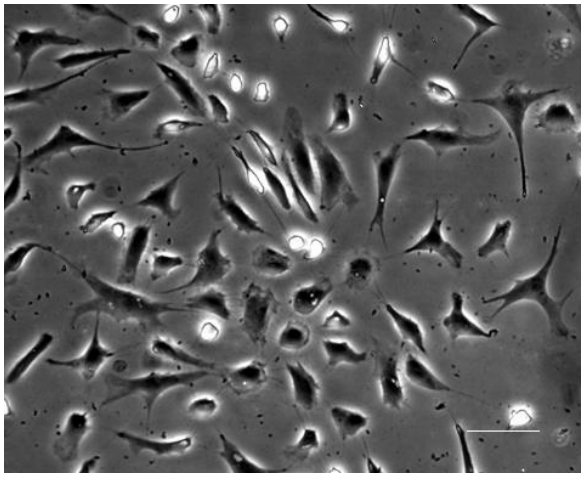

Fig. 3-5 Phase contrast image of BAECs after trypan blue stain
BAECs are on the polyacrylamide deformable substrate, Bar = 20 μm, N=11

3.1.4. Concentration of the Marker Beads

Concentration of the beads in the polyacrylamide gel is shown in Table 3-2. R^2 value close to 1.0 confirmed that the Beer-Lambert law works well not only for the acrylamide monomer solution but also for the polyacrylamide hydro-gel (Fig. 3-6).

Table 3-2. Concentration of the beads measured with spectrophotometer

Group	C (#/mL)	SD (#/mL)
Sonicated	53.6×10^{11}	0.74×10^{11}
Unsonicated	52.5×10^{11}	2.39×10^{11}

0.5% acrylamide, 0.1% bis-acrylamide, N=3 for each group
Filtered with 0.22-μm syringe driven filter before polymerization
C: Concentration of the beads (number per mL)
SD: Standard deviation

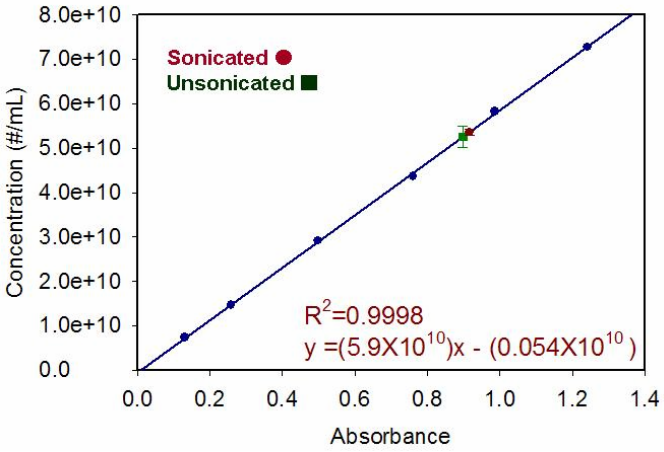

Fig. 3-6. Concentration of beads in the polyacrylamide gel
Blue line: standard curve of the absorbance and the concentration
Red circle and error bar: sonicated group
Green square and error bar: unsonicated group
N=3 for each group

Since the concentration of the beads, obtained from image processing program, varies with the threshold value (Fig. 2-11), it is important to determine the threshold value on a physical basis. For this purpose, image processed beads concentration was plotted against a range of cut-off values (candidates of threshold value). From the measured known concentration of 5.46×10^{10} /mL, the threshold value was determined to be 0.023 (Fig. 3-7). (Fig. 3-7). It is to be noted this threshold value lies in a near plateau region in which the concentration does not vary significantly with the threshold value.

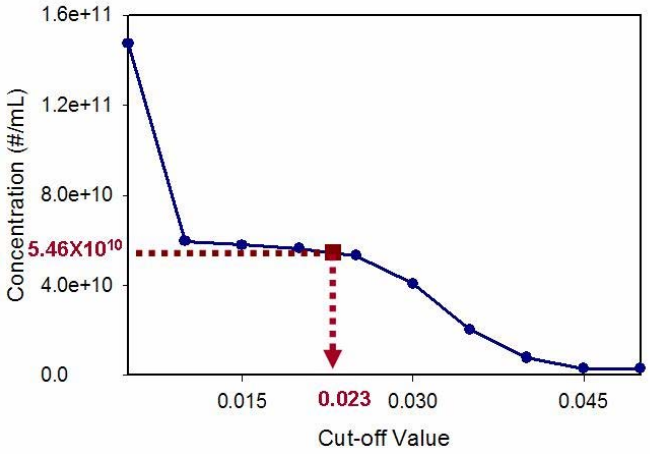

Fig. 3-7. Deciding threshold value from the measured concentration of the bead
Blue: Bead concentration calculated by image processing
Red: Bead concentration measured in the experiment

3.1.5. Diameter of Fluorescent Beads

Since what we detect under the fluorescence microscope in the polyacrylamide substrate is not the light reflected from the polystyrene beads, but the fluorescence light emitted from the TRITC (Tetramethyl Rhodamine Iso-Thiocyanate) molecules in the beads, the physical diameter and the image-processed diameter can be different. The mean diameter of the fluorescence beads determined with image-processing procedure was about 2~3 times larger (0.5~0.6 μm) than that of the physical diameter of beads (0.2 μm). The diameter of the beads determined with image processing procedure showed a normal distribution (Fig. 3-8).

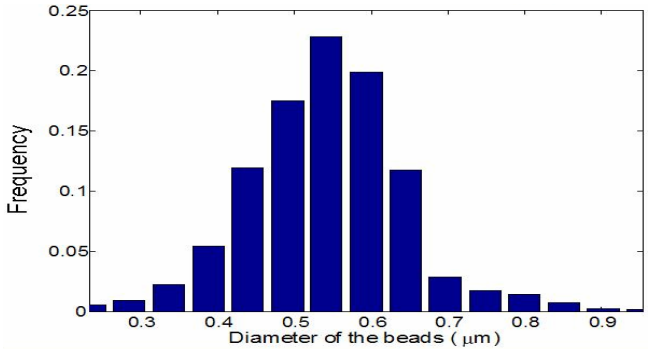

Fig. 3-8. Frequency distribution of bead diameter
Total number of the beads is normalized to 1

3.1.6. Thickness of Polyacrylamide Substrate

Since the brightness of the bead is at a maximum when the location coincides with the objective lens focus, the brightest plane (plane with maximum intensity) is conditioned to be where the bead is located. Therefore, we determined the position of the bead by tracking its brightness at each plane to determine the maximum intensity profile across the thickness.

With this method, the top of the polyacrylamide substrate was determined with high accuracy from the Z-directional brightness change of the beads located at the top. The bottom of the substrate was determined similarly, and the thickness was calculated from the Z position of the top and bottom obtained. Typically, gels with 15-25 μm thickness were casted from 6-9 μL of the acrylamide monomer solution.

3.1.7. Bead Distribution across the Thickness

Mapping of the distribution of beads across the deformable substrate showed that the beads are evenly distributed except at the top and bottom of the gel (Fig. 3-9). At these boundaries, the concentrations of the beads were higher.

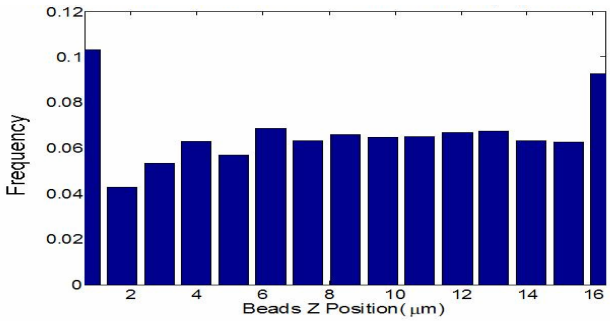

Fig. 3-9. Frequency distribution of the beads across the thickness (Z)
Total number of the bead is normalized to 1.
Z=0μ: Polyacrylamide gel top where polyacrylamide interfaces with the cells
Z=16.4μ: Polyacrylamide gel bottom where it is attached on the glass coverslip

3.2. 3D Traction Force Fields of BAEC

The traction force of the BAEC on the polyacrylamide substrate was measured (Fig. 3-10). The migration speed was sufficiently low so that no cell polarization (between front and tail of the cell) was observed.

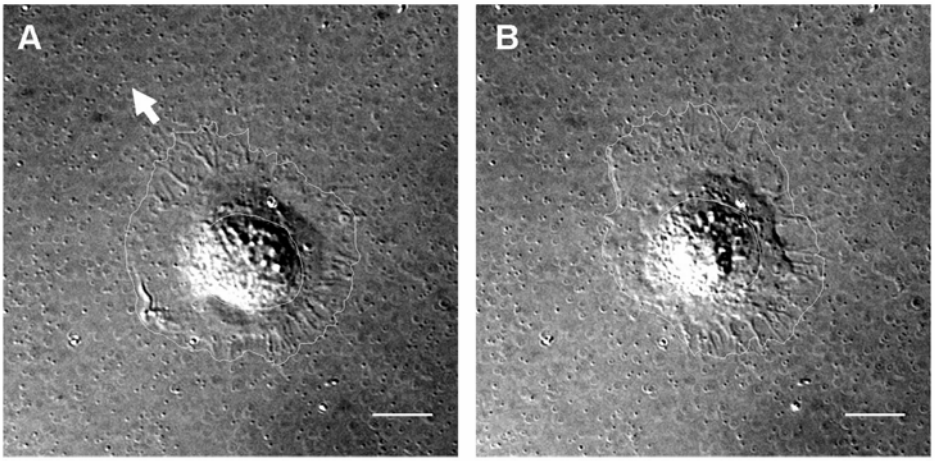

Fig. 3-10. DIC images of migrating BAECs
A: at t=0, Arrow: migration direction, B: at t = 30 min. Bars = 10 μm
The migration speed measured from nucleus movement was 0.168 μm/min

3.2.1. 3D Movement of the Marker Beads

A. At the Top plane

Movement of the marker beads at the top plane (Z = 0, at the interface with BAEC) is shown in Fig. 3-11B. The direction of bead displacement (from red to green) is generally toward the cell center. Beads far from the cell show no movement (yellow colored after merging of red and green). Large displacements are concentrated at the edge of the cell. Small displacements are observed under the nucleus (Fig. 3-11B).

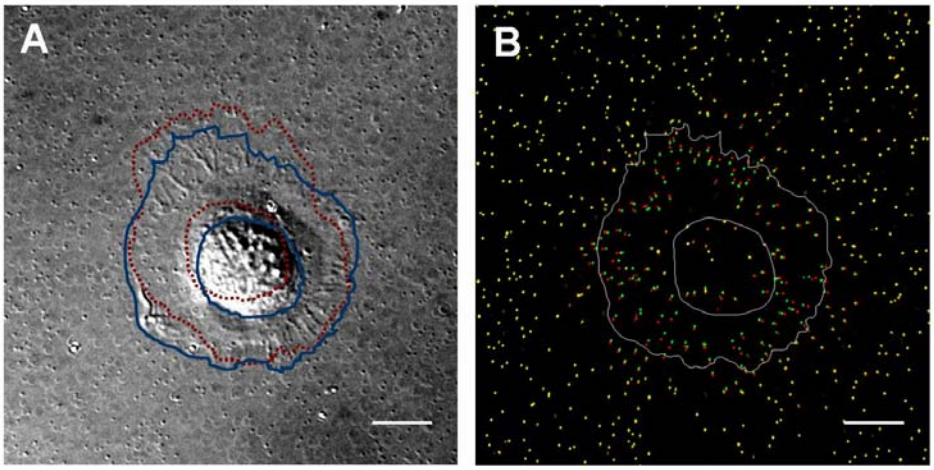

Fig. 3-11. DIC and merged fluorescent beads images at the top
A: DIC image (Bar = 10 μm)
Blue line: cell boundary and nucleus at t = 0
Red line: cell boundary and nucleus at t = 30 min
B: Merged TRITC beads image (Bar=10 μm)
White line: cell boundary and nucleus at t = 0
Bead movement is from red to green
Yellow beads: Merged bead color shows no bead movement

B. At the Bottom Plane

Since the glass coverslip prevents the displacement of the polyacrylamide substrate, no movements of the marker beads were observed at the bottom plane (Z=16.4 μm) (Fig. 3-12).

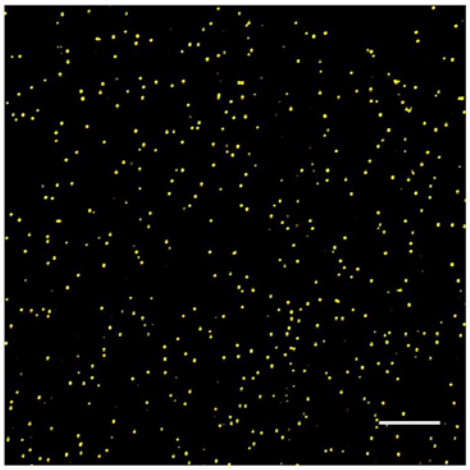

Fig. 3-12. Merged fluorescent beads image at the bottom
Yellow beads: Merged bead color shows no bead movement (Bar = 10 μm)

C. Under the Nucleus

Fig. 3-13A shows the movement of the beads in the Z-direction, which was taken from the diagonal line drawn on the top view in Fig. 3-13B. The circles show the location of the same beads in different figures. The Z-direction view shows purely downward movement (W>0) of the beads (Fig. 3-13A) under the nucleus (Fig 3-13C). No tangential movement (DispXY≅0) was observed at the merged yellow image of top view image under the nucleus (Fig. 3-13B).

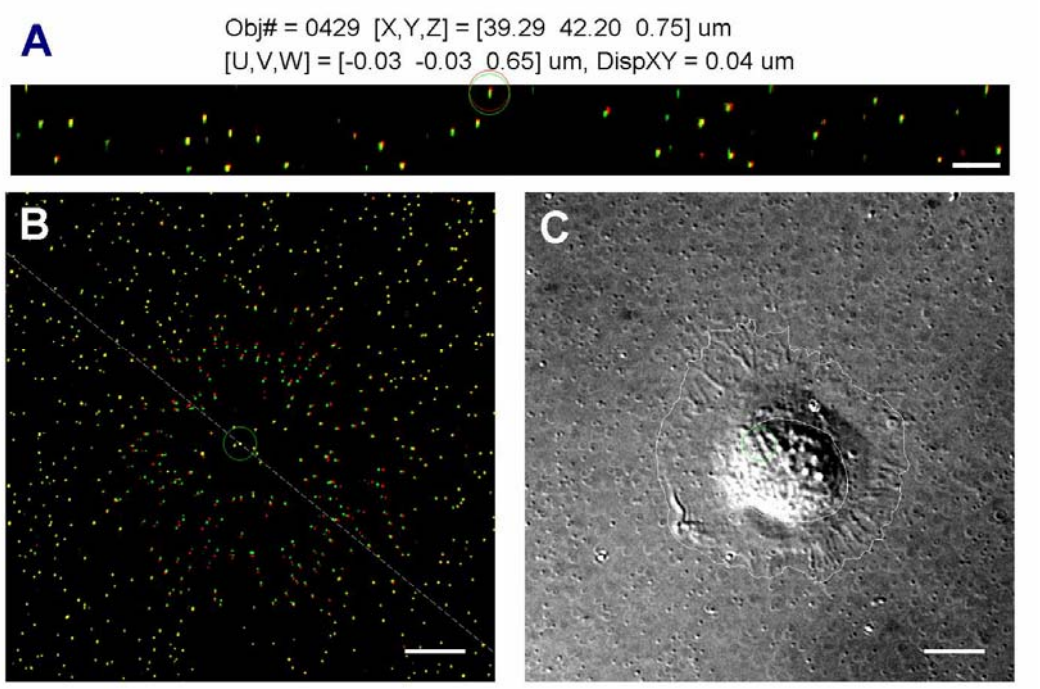

Fig. 3-13. Downward movement of the beads located under the cell nucleus
A: Side (Z) view of the polyacrylamide substrate across the line in B
B: Top view (XY) of the beads with section line
C: Top view (XY) of the cell
Circles show the positions of the bead common to different figures
Red = bead image without BAEC, Green = bead image with BAEC
U, V, W = Displacement of the bead in the X, Y, Z direction
DispXY = Magnitude of tangential displacement [U, V]
Bar(A) = 5 μm, Bar(B,C,D) = 10 μm

D. At the Cell Edge

Upward diagonal bead movements (W<0, large DispXY) are observed at the edge of the BAEC (Fig 3-14C). Large tangential (large DispXY) movement of the beads toward the cell center is shown in the top-view image of the beads (Fig. 3-14B). Upward movement of the beads (from red to green) is visualized in the side (Z) sectional view (Fig. 3-14A).

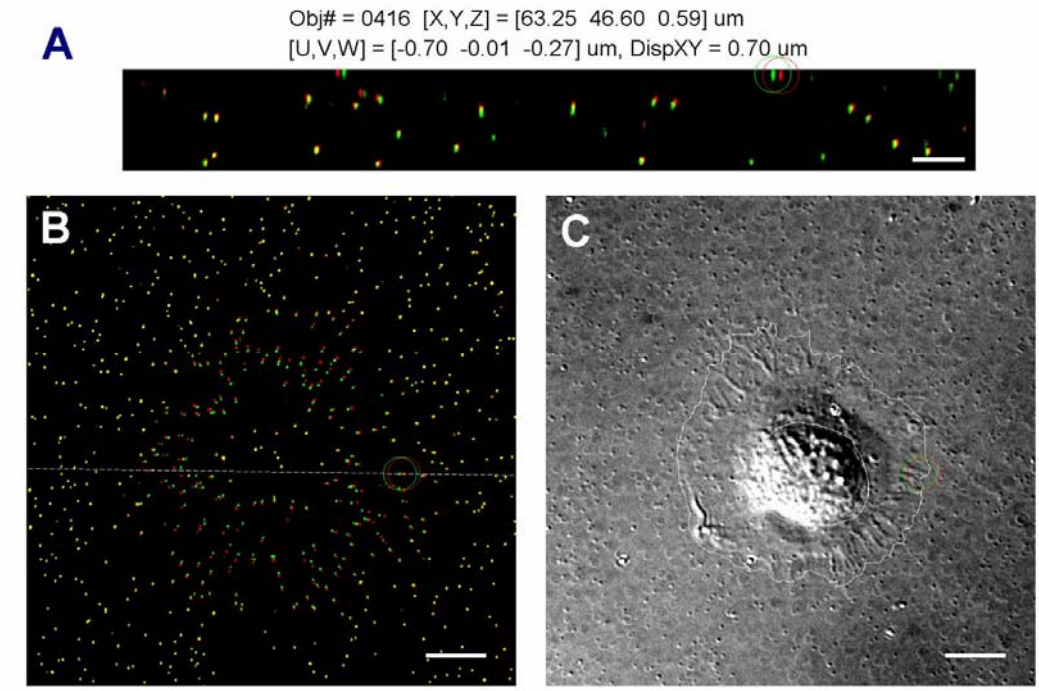

Fig. 3-14. Upward movement of the beads at the cell edge
A: Side (Z) view of the polyacrylamide substrate across the line in B
B: Top view (XY) of the beads with section line
C: Top view (XY) of the cell
Circles show the positions of the bead common to different figures
Red = bead image without BAEC, Green = bead image with BAEC
Bar(A) = 5 μm, Bar(B,C,D) = 10 μm

E. Regions between the Nucleus Edge and Cell Edge

Downward diagonal (W>0, large DispXY) bead movement was observed in regions between the edge of the nucleus and edge of the BAEC (Fig 3-15C). Tangential movement of the beads toward the cell center is shown (Fig. 3-15B), but its magnitude is smaller than that of the beads located at the cell edge. Downward movement (from red to green) of the beads is visualized in the side sectional view (Fig. 3-15A).

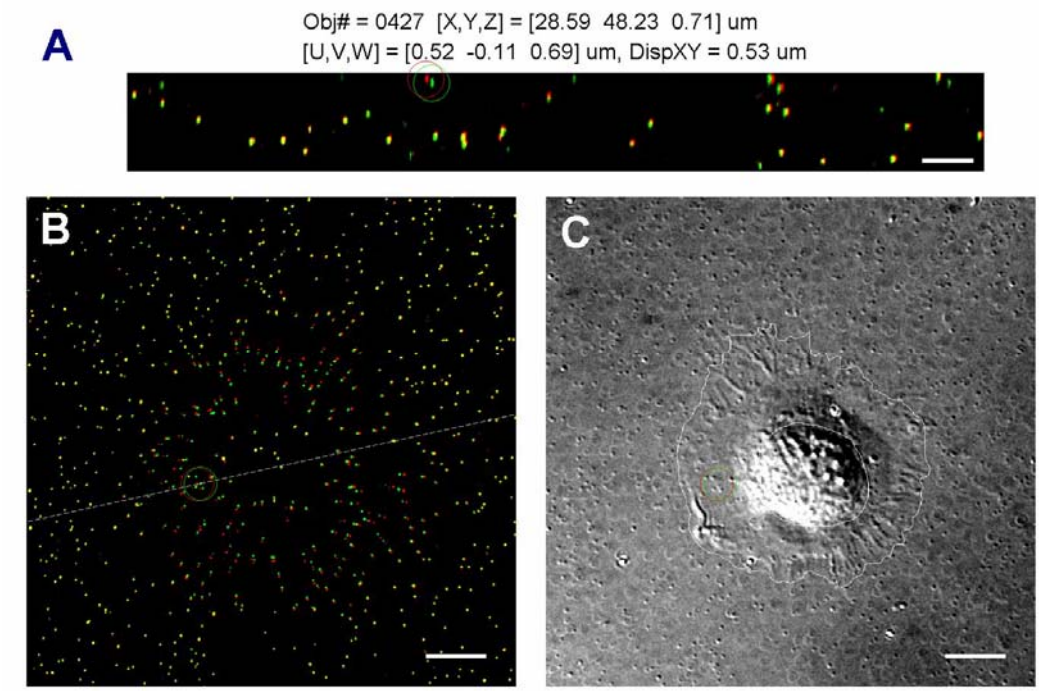

Fig. 3-15. Downward movement of the beads in regions between the cell edge and the nucleus edge

A: Side (Z) view of the polyacrylamide substrate across the line in B
B: Top view (XY) of the beads with section line
C: Top view (XY) of the cell
Circles show the positions of the bead common to different figures
Red = bead image without BAECs, Green = bead image with BAECs
Bar(A) = 5 μm, Bar(B,C,D) = 10 μm

3.2.2. Reconstructed Surface of Polyacrylamide Substrate

The surface of the polyacrylamide substrate deformed by BAEC was reconstructed from the data on the displacement of the marker beads (Fig. 3-16A). Topology of the deformed substrate is visualized by the side cut views (Fig. 3-16B, C). It can be seen that the polyacrylamide substrate is pulled up at the cell edge (blue) and pushed down under the cell nucleus (red).

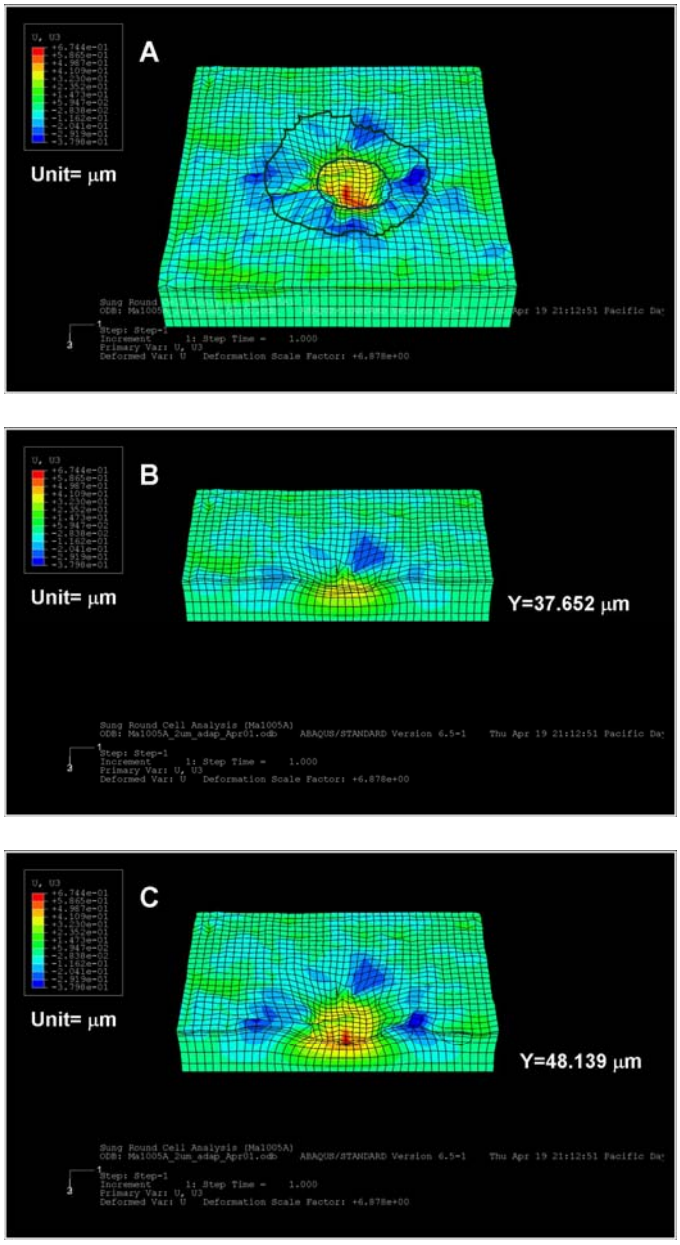

Fig. 3-16. Surface of the polyacrylamide substrate deformed by BAEC
A: Whole view of the substrate
B: Side cut view of the substrate (Y = 37.7 μm)
C: Side cut view of the substrate (Y = 48.1 μm)
U_3 = W: Z directional displacement of the substrate
1, 2, 3 = X, Y, Z: Direction of the spatial coordinates
Mesh size in X, Y direction = 2 μm
Thickness of the deformable substrate = 16.4 μm

3.2.3. Resolution of Displacement Measurement

The resolution of displacement measurements with the 5NVA method was evaluated (Table

3-3) following the procedure mentioned under Materials and Methods. Displacements of the beads close to the glass slide were very close to zero. The resolution was found to be 35.5 nm.

Table 3-3. Resolution of the bead displacement measurement

	u_x	u_y	u_z	Mag
m	1.20×10^{-16}	4.53×10^{-16}	-4.21×10^{-16}	1.204×10^{-16}
SD	0.0132	0.0128	0.0303	0.0355

u_x, u_y, u_y = displacement of the beads in each coordinates (Unit = μm)
m = mean of the displacement, SD = standard deviation

3.2.4. 3D Displacement Field

3D deformation of the polyacrylamide substrate induced by the migrating BAEC was measured. Tangential displacement (Fig. 3-17A) and normal displacement fields (Fig. 3-17B) were evaluated at 0.4 μm below the top of the substrate. Centripetal tangential displacement field was observed (Fig. 3-17A). BAEC pulled up the substrate at the cell edge, but pushed down under the nucleus (Fig. 3-17B). Normal displacement was comparable with tangential displacement in magnitude, being on the order of 1 μm. Both tangential and normal displacements approached zero rapidly with increasing distance of the bead position from the BAEC.

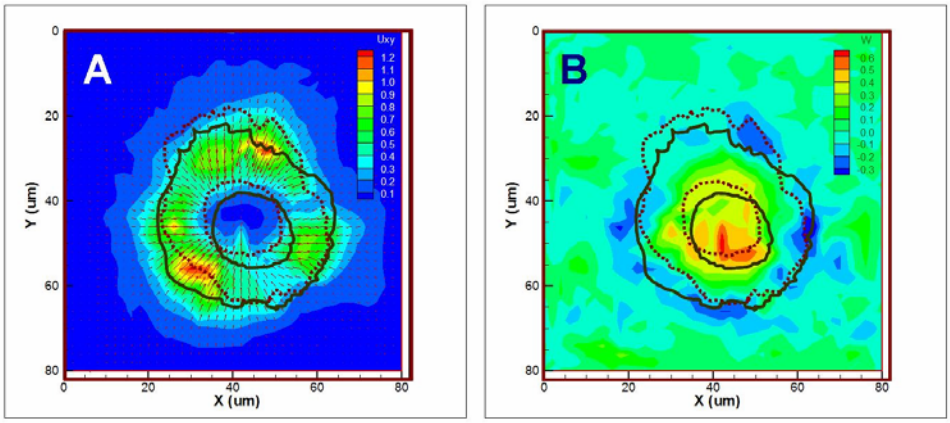

Fig. 3-17. Contour map of 3D displacement fields at 0.4 μm below the top of substrate
A: Tangential (XY directional) displacement field (Unit = μm)
Arrow: direction of the displacement
B: Normal (Z directional) displacement field (Unit = μm)
+: Downward (pushed down) direction, -: Upward (pulled up) direction
Dark green solid lines: Boundaries of cell and nucleus of BAEC at t = 0
Dark red dotted lines: Boundaries of cell and nucleus of BAEC at t = 30 min

3.2.5. 3D Traction Force Field

The 3D traction force field induced by the contraction of BAEC was computed from the measured 3D displacement field (Fig. 3-18). Centripetal tangential traction force pattern was observed. Large tangential forces were observed at the edge, while small tangential forces were found under the nucleus. Upward normal force was observed at the cell edge while downward normal force was dominant under the nucleus. Normal traction force was comparable with tangential traction force, with the order of magnitude of 1 kPa. Interestingly, the largest downward traction force was not located under the center of the nucleus (mostly it is located at the edge of the cell nucleus). Both tangential and normal traction forces became zero more rapidly than displacement as the distance of the bead position from the BAEC became longer. Other experimental results from BAECs (N=10) have supported these 3D traction force fields findings.

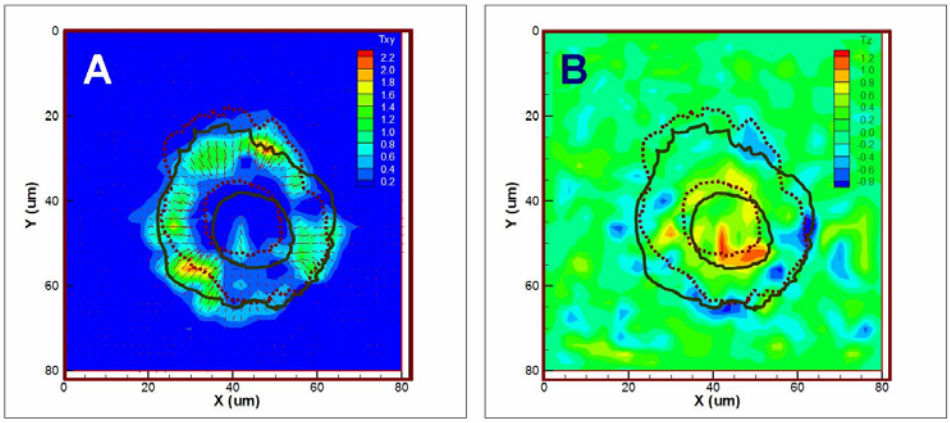

Fig. 3-18. Contour map of 3D traction force field at 0.4 μm below the top
(A) Tangential (XY directional) traction force field (Unit = kPa)
Arrow: direction of the traction force
(B) Normal (Z directional) traction force field (Unit=kPa)
+: Downward (pushed down) direction, -: Upward (pulled up) direction
Dark green solid line: Boundary and nucleus of BAEC at t=0
Dark red dotted line: Boundary and nucleus of BAEC at t=30 min

3.3. 3D Traction Force and FA Dynamics of BAEC (Spatial Analysis)

The traction force of the migrating BAEC transfected with GFP-paxillin was measured (Fig. 3-19). Migration speed was large in this case, and polarization of the BAEC with cell front and tail was observed.

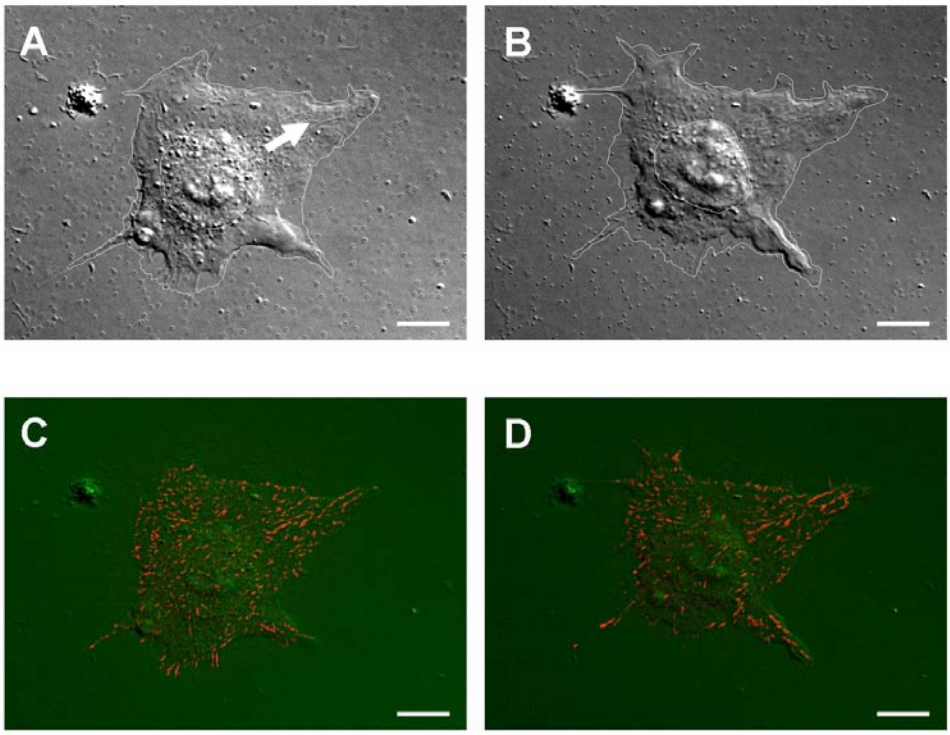

Fig. 3-19. Migrating BAEC transfected with GFP-paxillin
A: DIC image at t=0, B: DIC image at t = 10 min (Bars = 10 μm)
C: GFP-paxillin image merged with DIC image at t = 0
D: GFP-paxillin image merged with DIC image at t = 10 min
Arrow: migration direction
The migration speed measured from nucleus movement was 0.498 μm/min

3.3.1. Reconstructed Surface of the Deformable Substrate

Surface of the polyacrylamide substrate deformed by BAEC (Fig. 3-19) was reconstructed from the data on the displacements of the marker beads (Fig. 3-20A). Topology of the deformed substrate visualized by the side (Z) view (Fig. 3-20B) shows that the polyacrylamide substrate is pulled up at the cell edge (blue) and pushed down under the cell nucleus (red). Substrate

deformation by FA-transfected BAEC was similar to that by BAEC without FA transfection (Fig. 3-16).

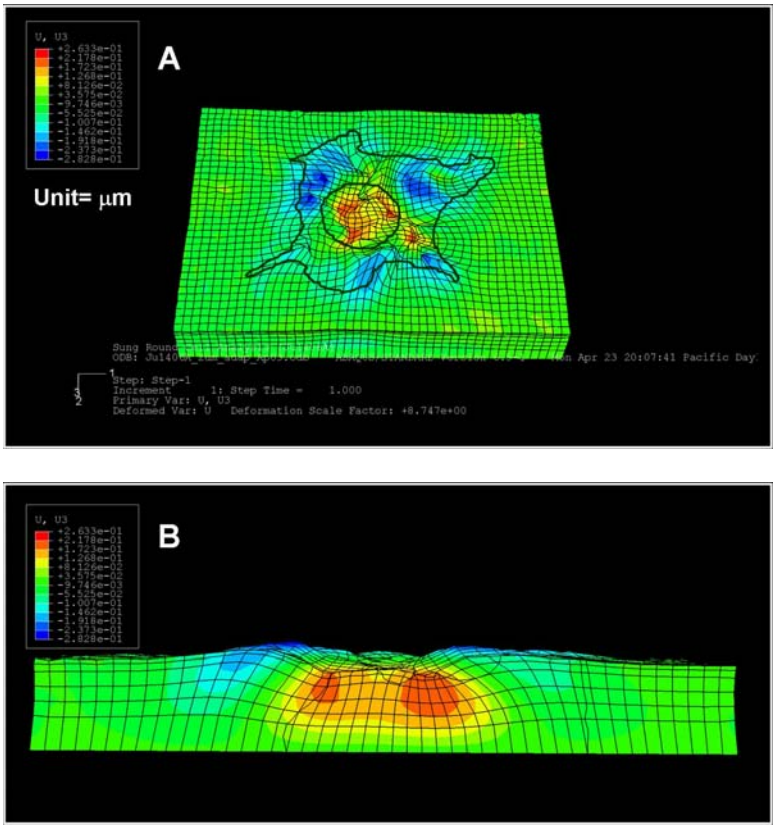

Fig. 3-20. Surface of the polyacrylamide substrate deformed by BAEC
A: Whole view of the substrate
B: Side cut view of the substrate
U3 = W: Z directional displacement of the substrate
1, 2, 3 = X, Y, Z: Directions of the spatial coordinates
Mesh size in X, Y direction = 2 μm
Thickness of the deformable substrate = 12.4 μm

3D deformation of the polyacrylamide substrate induced by the migrating BAEC transfected with GFP-paxillin was measured. Tangential displacement (Fig. 3-21C) and normal displacement fields (Fig. 3-21C) were evaluated at 0.4 μm below the top of the substrate. Centripetal tangential displacement field was observed (Fig. 3-21C). BAEC pulled up the substrate at the cell edge, but pushed down under the nucleus (Fig. 3-21D). Normal displacement

was comparable with tangential displacement with the order of magnitude of 1 μm. Both tangential and normal displacements became zero rapidly with increasing distance from the BAEC. These results are consistent with those obtained from the untransfected BAEC. Large tangential and upward normal displacements were observed at the regions where the cell had newly forming lamellapodia (Fig. 2-21CD).

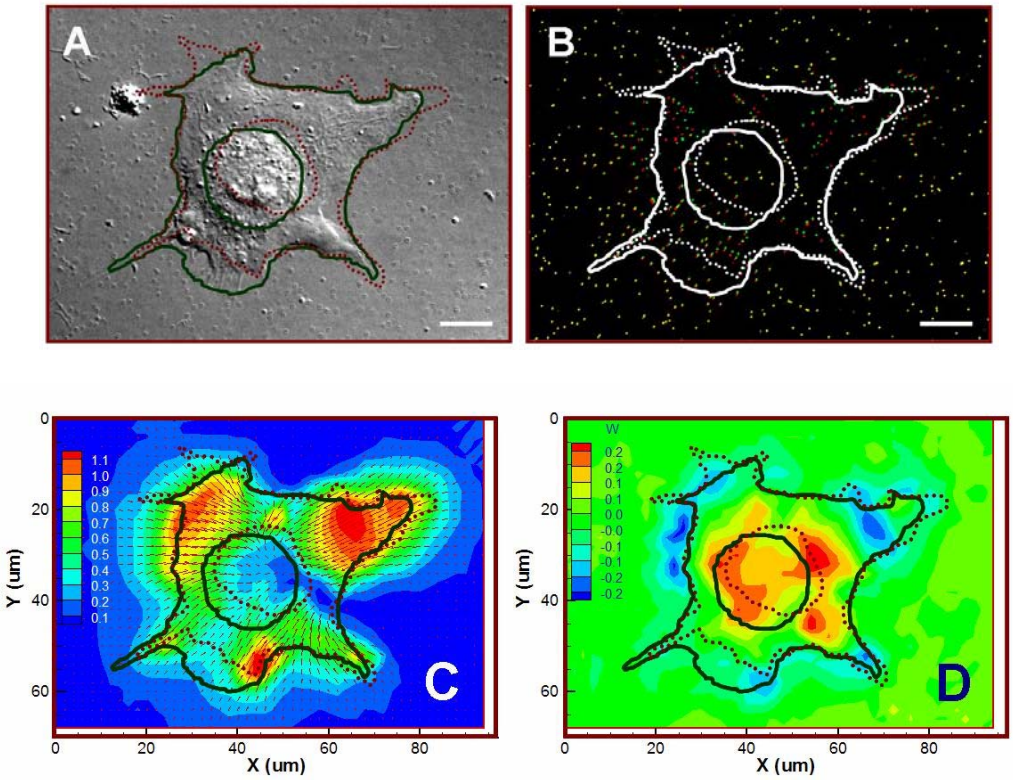

Fig. 3-21. 3D displacement field by BAEC transfected with GFP-paxillin
A: DIC image at t=0 (Bar=10 μm)
B: Merged fluorescent beads image at t=0
Arrows: Directions of the tangential traction stress vector
C: Tangential displacement field at t=0 (Unit=μm)
D: Normal displacement field at t=0 (Unit=μm)
+: Downward normal displacement
-: Upward normal displacement
Dark green solid lines: Boundaries of cell and nucleus at t=0 (A, C, D)
Dark red dotted lines: Boundaries of cell and nucleus at t=10 min (A, C, D)
White solid lines: Boundaries of cell and nucleus at t=0 (B)
White dotted lines: Boundaries of cell and nucleus at t=10 min (B)

3.3.3. 3D Traction Force Field

3D traction force field induced by contraction of BAEC was computed from the measured 3D displacement field (Fig. 3-21). Centripetal tangential traction force pattern was observed. Large tangential force is observed at the edge, while small tangential force is shown under the nucleus. Upward normal force was observed at the cell edge while downward normal force was dominant under the nucleus. Normal traction force was comparable with tangential traction force with the order of magnitude of 1 kPa. Largest downward traction force was located at the region between the center and edge of the cell (mostly at the edge of the cell nucleus). Both tangential and normal traction force became zero more rapidly than displacement as the distance of the position from the BAEC became longer. These results are consistent with those obtained from the untransfected BAEC. Large tangential traction forces and upward normal forces were involved at the regions where the cell had newly forming lamellapodia (Fig. 2-22AB).

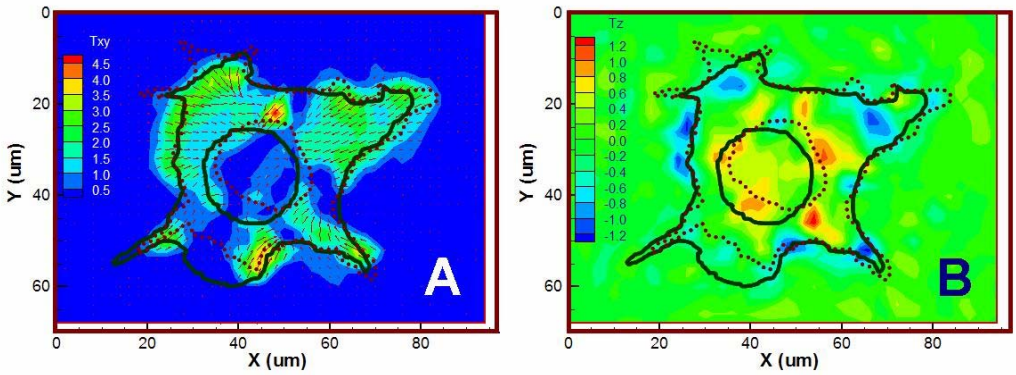

Fig. 3-22. 3D traction force field by BAEC transfected with GFP-paxillin

A: Tangential traction force at t=0 (Unit=kPa)
Arrows: Direction of the tangential traction stress vector
B: Normal traction force at t=0 (Unit=kPa)
+: Downward normal traction force direction
-: Upward normal traction force direction
Dark green solid lines: Boundaries of cell and nucleus of BAEC at t = 0
Dark red dotted lines: Boundaries of cell and nucleus of BAEC at t = 10 min

3.3.4. 3D Traction Force Field and FA Dynamics

Three regions were categorized according to different FA dynamics of BAEC (Fig. 3-23). Forces at the location of FAs were determined from the computed traction force field (Fig. 3-22) and FA characteristics quantified, as mentioned in Materials and Method (Section 2.9).

Other experimental results from BAECs transfected with GFP-paxillin (Two experiments, N=6) have supported the findings below.

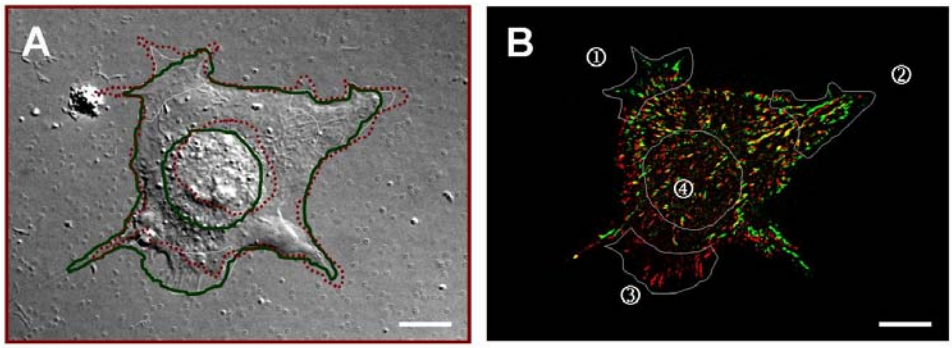

Fig. 3-23. FA dynamics of BAEC transfected with GFP-paxillin
A: DIC image at t = 0 (Bar = 10 μm)
Dark green solid lines: Boundaries of cell and nucleus at t = 0
Dark red dotted lines: Boundaries of cell and nucleus at t = 10 min
White solid lines: Regions of different FA dynamics (B)
B: Merged GFP-paxillin images
Red FAs: FAs at t = 0
Green FAs: FAs at t =10 min
White solid lines: Regions of different FA dynamics
Region①: New lamellapodia forming region #1
Region②: New lamellapodia forming region #2
Region③: Retracting region
Region④: Under the nucleus

A. Region of new lamellapodia formation

FAs in the new lamellapodia forming region (Regions ① and ② in Fig 3-23B) at the cell migrating front (Fig. 3-23A) were dynamic as they turned over or moved long distance (Fig. 3-23B). In this region, upward normal forces were dominant on FAs (Fig. 3-24).

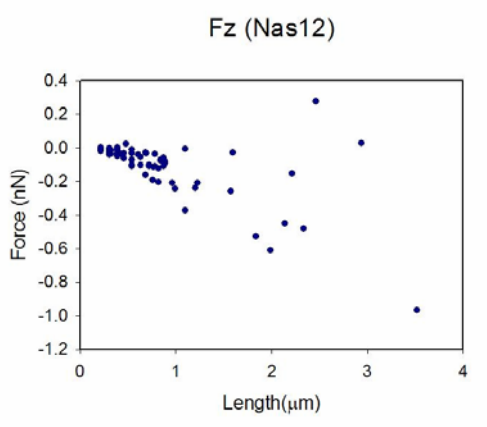

Fig. 3-24. Normal force vs. FA length in the new lamellapodia forming region
Linear plot, +: Downward direction, -: Upward direction, (Unit = nN)

Large tangential forces were exerted on the FAs in this region. A linear relationship between the FA length and force was observed in log-log plots for both tangential and downward normal forces (Fig. 3-25).

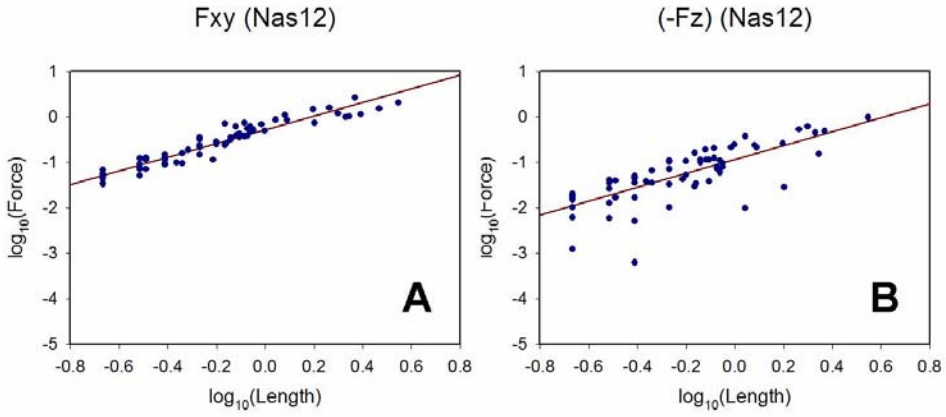

Fig. 3-25. Force vs. FA length in the new lamellapodia forming region
A: Tangential force
Regression line: y = 1.51 x + (-0.28), R^2 = 0.92
B: Normal force (Only for FAs with upward forces)
Regression line: y = 1.53 x + (-0.94), R^2 = 0.59
Log-Log plot, +: Downward direction, -: Upward direction, (Unit = nN)

B. Retracting region

. FAs in retracting region (Region ③ in Fig 3-23B) at the rear of the migrating cell (Fig. 3-23A) were dynamic as they turned over (Fig. 3-23B). In this region, upward normal force was dominant on FAs (Fig 3-26).

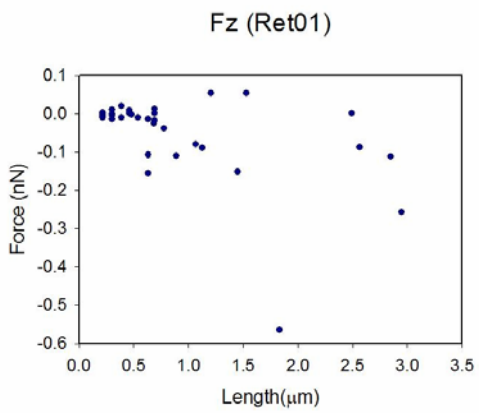

Fig. 3-26. Normal force vs. FA length in the retracting region
Linear plot, +: Downward direction, -: Upward direction, (Unit = nN)

Large tangential force was exerted on the FAs. A linear relationship between the FA length and force was observed in log-log plots for both tangential and upward normal force (Fig. 3-27). In this region, the relation between FAs and force was similar to that in the new lamellapodia-forming region, except that the force was smaller and the linear relationship is not as distinct as that in the new lamellapodia-forming region.

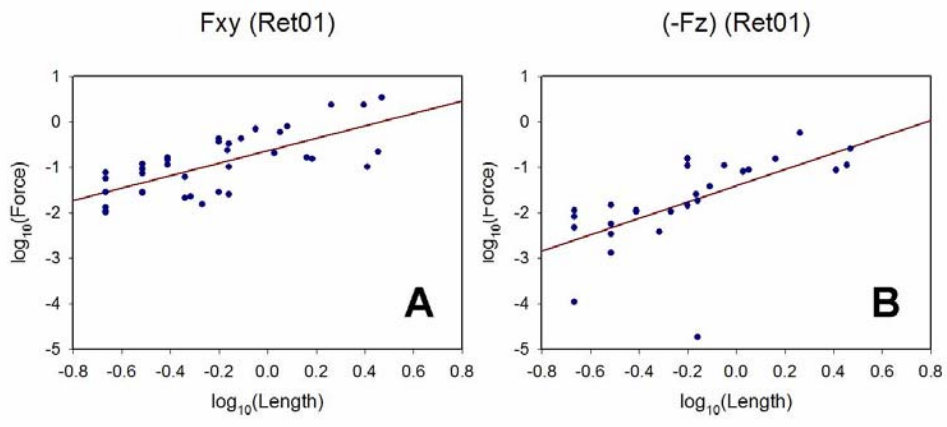

Fig. 3-27. Force vs. FA length in the retracting region
A: Tangential force
Regression line: y = 1.37 x + (-0.63), R^2 = 0.51
B: Normal force (Only for FAs with upward forces)
Regression line: y = 1.80 x + (-1.41), R^2 = 0.39
Log-Log plot, +: Downward direction, -: Upward direction, (Unit = nN)

C. Under the nucleus

FAs under the nucleus (Region④ in Fig 3-23B) and at the cell body (Fig. 3-23A) were stable, as there was no rapid change of position or size (Fig. 3-23B). In this region, downward normal forces were dominant on the FAs (Fig. 3-28). Smaller tangential forces were exerted on the FAs.

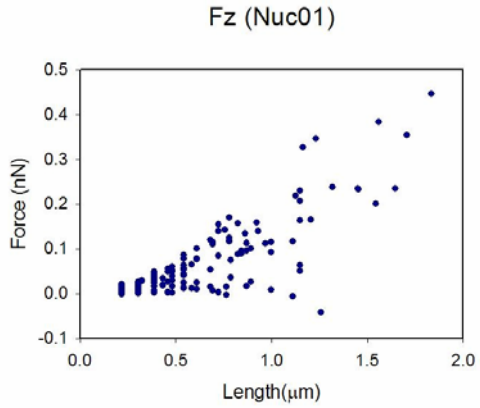

Fig. 3-28. Normal force vs. FA under the nucleus
Linear plot, +: Downward direction, -: Upward direction, (Unit = nN)

A linear relationship between the FA length and force was observed in log-log plots for both

tangential and normal forces (Fig. 3-29).

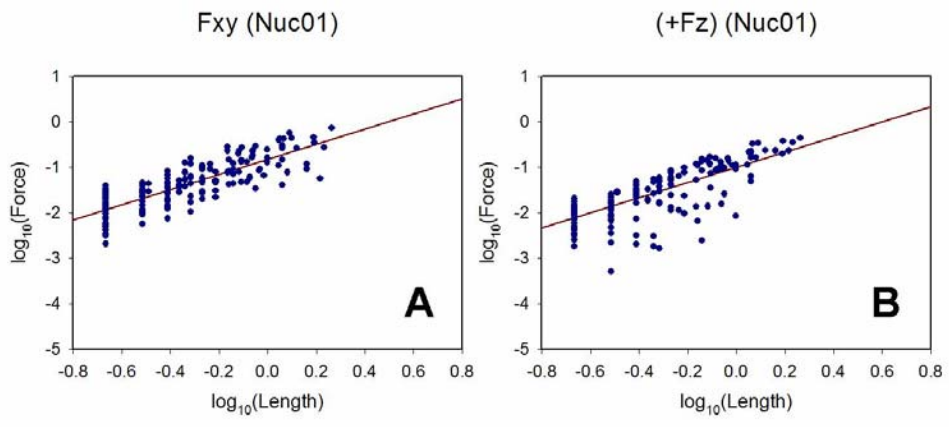

Fig. 3-29. Force vs. FA length under the nucleus
A: Tangential force
Regression line: y = 1.66 x + (-0.82), R^2 = 0.68
B: Normal force (Only for FAs with downward forces)
Regression line: y = 1.66x + (-1.00), R^2 = 0.58
Log-Log plot, +: Downward direction, -: Upward direction, (Unit = nN)

D. Comparison between regions

Forces on FAs in three different regions are compared (Fig 3-30). FAs at the new lamellapodia forming region experience large tangential forces and upward normal forces. FAs at the retracting region show similar behaviors, but the magnitude is smaller for both tangential and normal forces. FAs under the cell nucleus experience small tangential forces and the normal forces are downward, which is distinct from other regions.

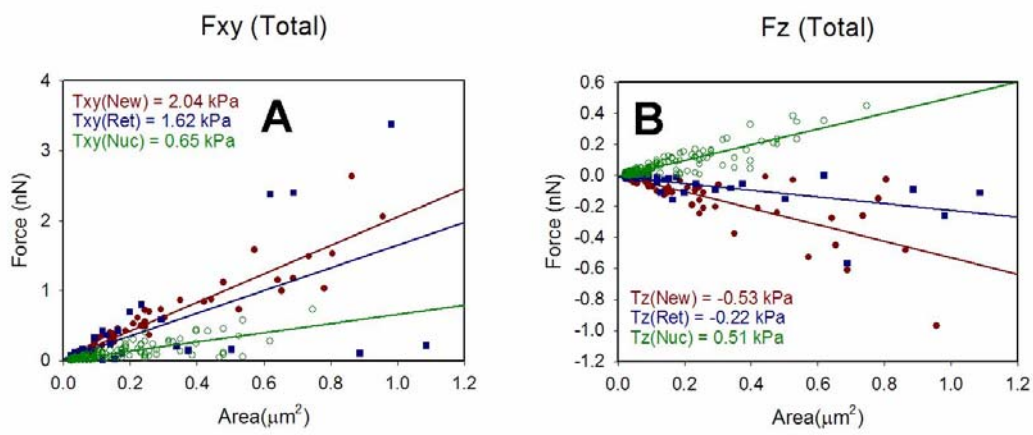

Fig. 3-30. Force vs. area of FA

A: Tangential force

Red line: $y = 2.04x + 0.017$, $R^2 = 0.90$

Blue line: $y = 1.62x + 0.029$, $R^2 = 0.38$

Green line: $y = 0.654x + 0.0019$, $R^2 = 0.63$

B: Normal force

Red line: $y = -0.530x - 0.0017$, $R^2 = 0.58$

Blue line: $y = -0.219x - 0.0082$, $R^2 = 0.36$

Green line: $y = 0.507x - 0.0061$, $R^2 = 0.79$

Lines: Regression line showing the force-area relationship in the FAs

Red: New lamellapodia-forming region

Blue: Retracting region, Green: Under the nucleus

Linear plot, +: Downward direction, -: Upward direction, (Unit = nN)

3.4. 3D Traction Force Field and FA Dynamics of BAEC (Time Analysis)

The traction force field was computed for BAEC transfected with GFP-FAK (Fig. 3-30), and FA dynamics of the GFP-FAK transfected BAEC was observed.

Except for the new lamellapodia-forming region and the retracted region, FAs did not move much in spite of the migration of the cell body in the forward direction. From the position change of cell nucleus and the filopodial filaments linked from the cell (Fig. 3-30E, See arrows), we could observe the cell movement and directional change.

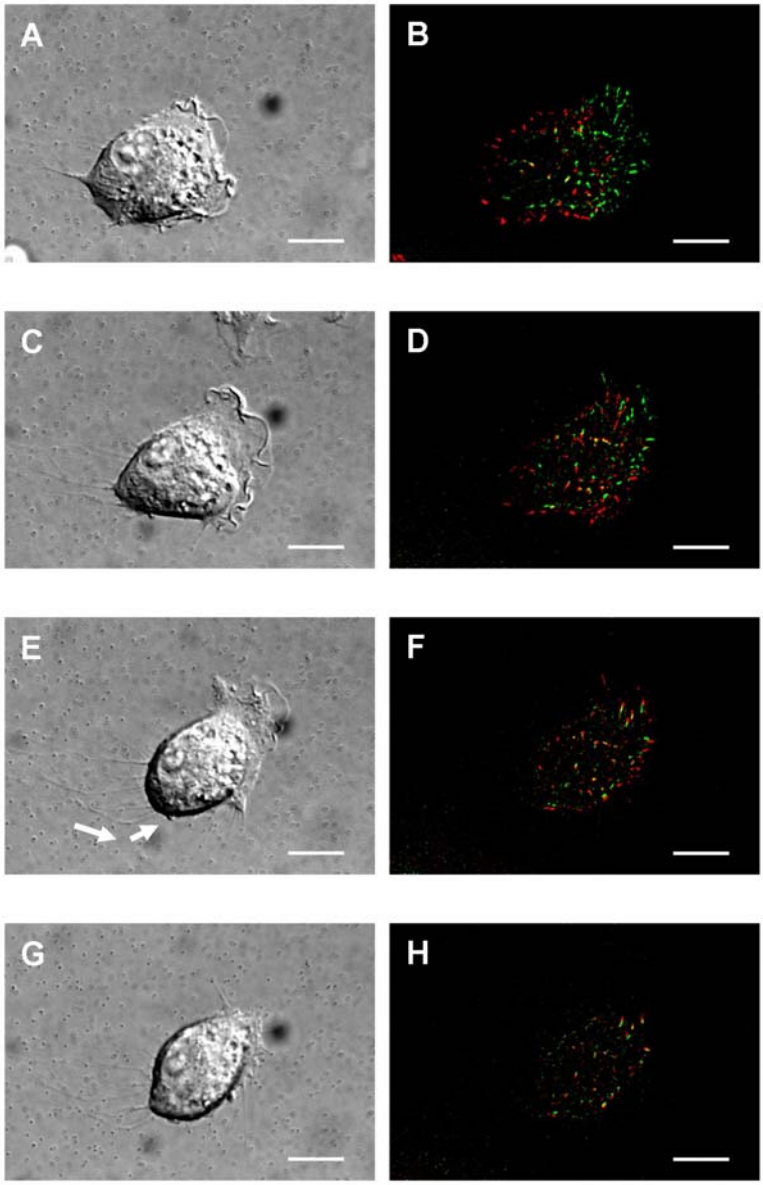

Fig. 3-30. Focal adhesions (FAs) dynamics of BAEC
DIC images at t=0 (A), 15m (C), 30m (E) and 45m (G), (Bars = 10 μm)
GFP-FAK images at t=0-15m (B), 15-30m (D), 30-45m (F) and 45-60m (H)
Red FAs: FA at previous time point
Green FAs: FA at next time point

3.4.1. 3D Displacement Field

Tangential and normal displacement fields of BAEC transfected with GFP-FAK (Fig. 3-30) were measured (Fig. 3-31).

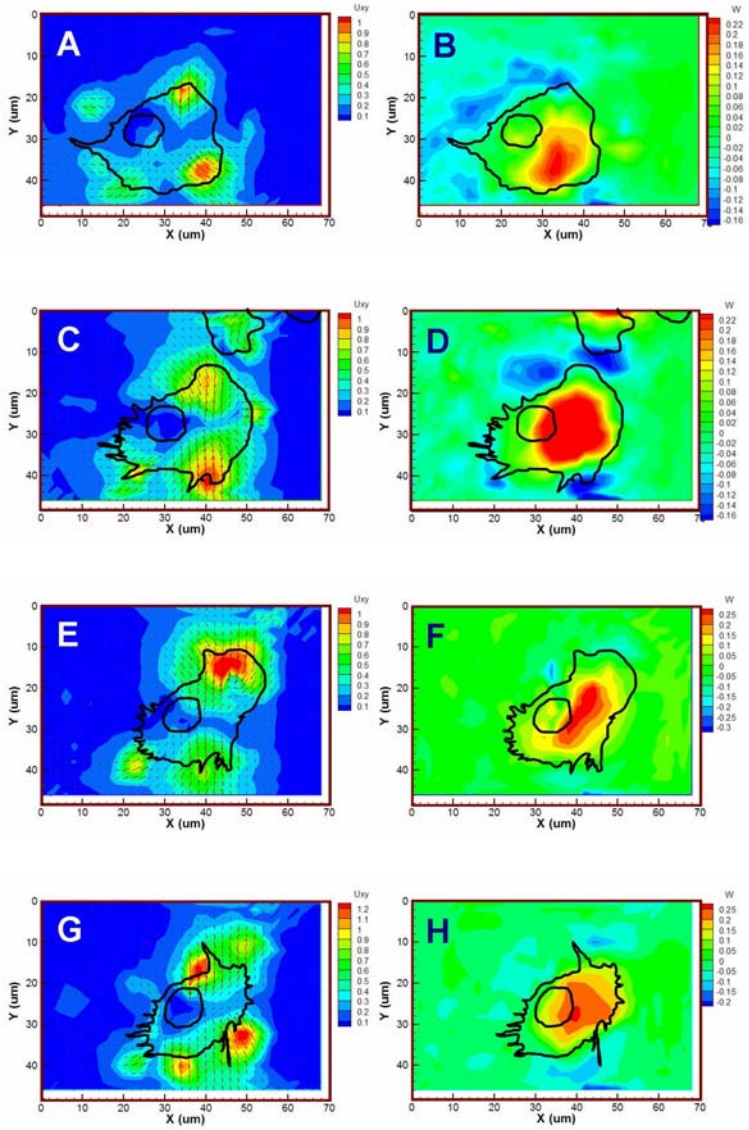

Fig. 3-31. 3D Displacement field of GFP-FAK transfected BAEC
Tangential displacement at t=0 (A), 15m (C), 30m (E) and 45m (G)
Normal displacement at t=0 (B), 15m (D), 30m (F) and 45m (H)
Arrows: Directions of the tangential displacement vector
Dark green solid lines: Boundaries of cell and nucleus at each time point
+: Downward normal direction, -: Upward normal direction

3.4.2. 3D Traction Force Field

Tangential and normal traction force fields (Fig. 3-32) of GFP-FAK-transfected BAEC were computed from the 3D displacement field (Fig. 3-31).

Cell migration directions were closely correlated with tangential traction force field pattern. Sequential changes in cell migration direction (Fig. 3-30 A, C, D) are accompanied by changes of polarized tangential displacements and traction forces (Fig. 3-31 A, C, D and Fig. 3-32 A, C, D). When the cell lost the polarization of traction forces, the migration stopped (Fig. 3-31 F, Fig. 3-32 F).

Downward normal force was dominant under the cell body. Upward normal force is mostly located at the cell edges. In some cases, filopodial filaments attached to the polyacrylamide substrate exerted upward normal forces at the places just outside the cell edges (Fig. 3-30 A, C, Fig. 3-31 B, D and Fig. 3-32 B, D).

These results are consistent well with those on untransfected BAEC and GFP-paxillin transfected BAEC, as described in Sections 3.2 and 3.3, respectively.

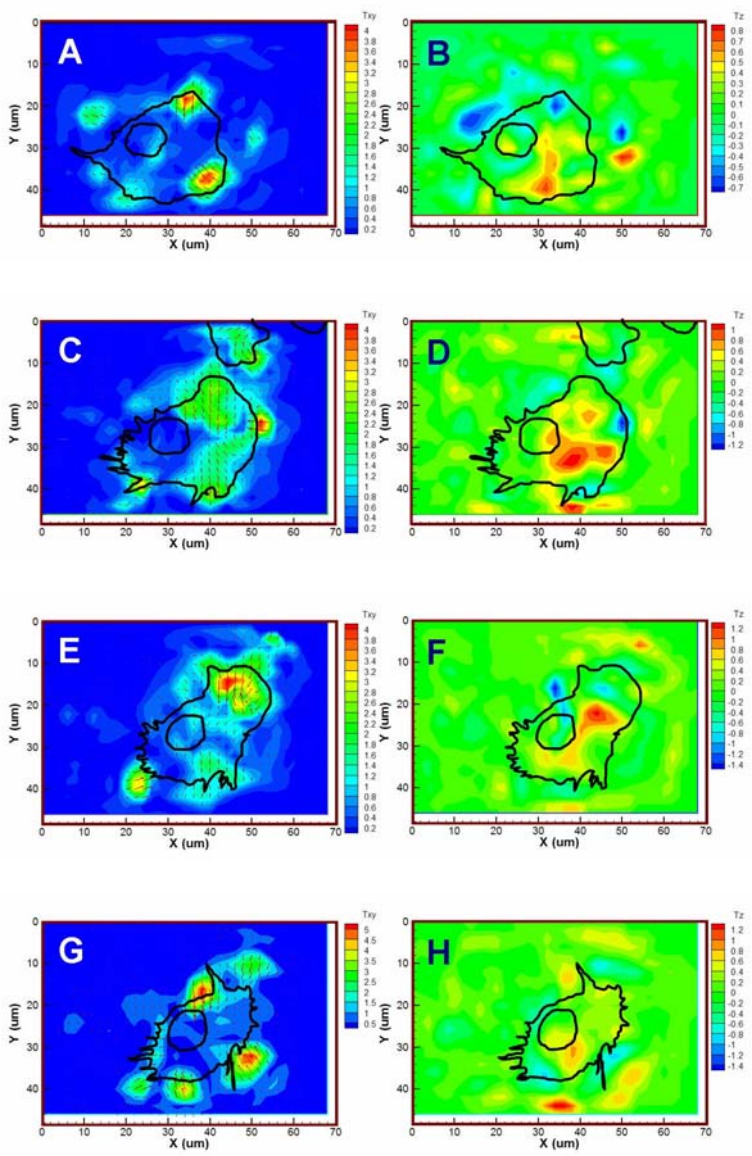

Fig. 3-32. 3D Traction force field of GFP-FAK-transfected BAEC
Tangential traction force at t=0 (A), 15m (C), 30m (E) and 45m (G)
Normal traction force at t=0 (B), 15m (D), 30m (F) and 45m (H)
Arrows: Directions of the tangential traction force vector
Dark green solid lines: Boundaries of cell and nucleus at each time point
+: Downward normal direction, -: Upward normal direction

3.4.3. 3D Traction Force and FA Dynamics

Dynamic FAs (FAs that traverse a long distance or undergo turnover) and stable FAs (FAs do not change their position and size) were tracked with time and the results are compared (Fig 3-33). FAs with unstable dynamics (Fig. 3-33 A, 1 and 2) experienced large upward normal forces and

rapid force changes with time (Fig. 3-33C and D Red and black). FAs with stable dynamics were located under the cell body but outside the nucleus (Fig. 3-33 A, 3); they experienced large downward normal forces, and the forces were maintained constant with time (Fig. 3-33C and D, Green). Other experimental results from BAECs transfected with GFP-FAK (Two experiments, N=6) support these findings.

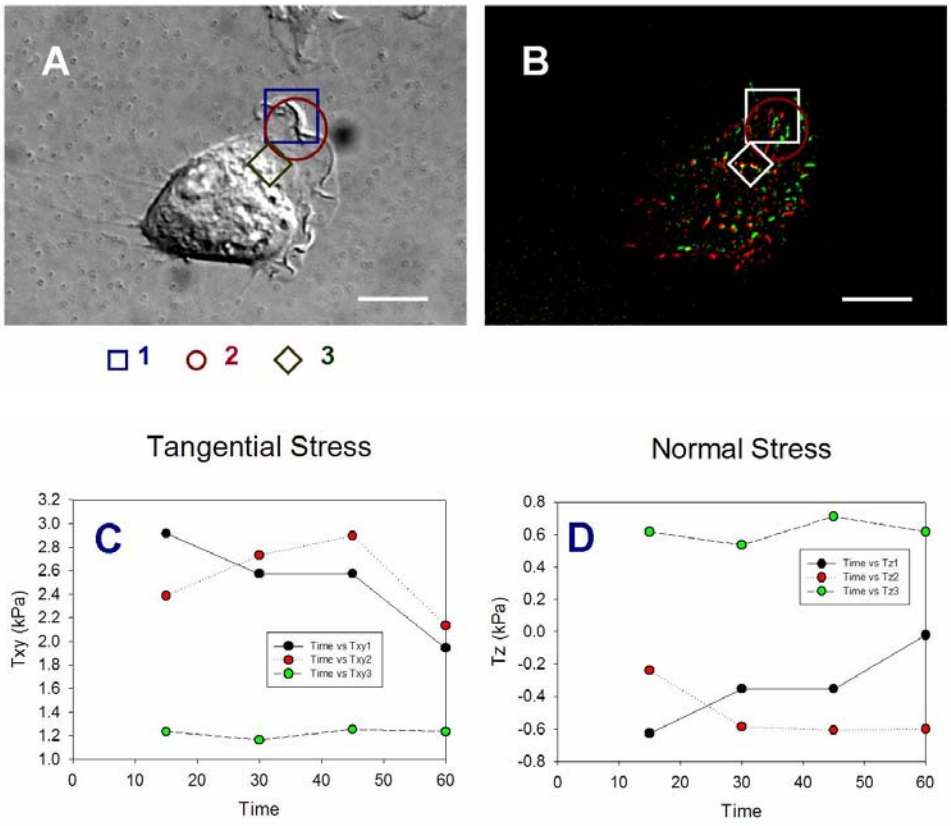

Fig. 3-33. Time course tracking of individual FAs of BAEC

A: DIC image

B: GFP-FAK images

Red FAs: FAs at t =15 min, Green FAs: FAs at t =30 min

FA 1, 2: Dynamic FAs located at the cell edge

FA 3: Stable FA located between nucleus edge and cell edge

C: Tangential traction force

D: Normal traction force

IV. DISCUSSION

I have developed a novel 3D traction force microscopy technique to measure the 3D traction forces, including the normal traction force, of live cells using the polyacrylamide deformable substrate method. I have characterized the polyacrylamide deformable substrate in terms of its materials properties, biocompatibilities, and marker bead concentrations (Section 4.1). I have developed the image processing algorithms and verified their applicabilities and resolutions (Section 4.2). I have also developed an improved 3D computational method to calculate the traction forces based on the FEM. This method has shown better performance in comparison to the methods used in previous studies (Section 4.3).

I have applied this new method to BAEC to determine 3D traction forces, including the normal force, and their relations with BAEC migration and FA dynamics (Section 4.4).

4.1. Characterization of Polyacrylamide Deformable Substrate

4.1.1. Elasticity of Polyacrylamide

Since stress relaxation test results (Section 3.1.1) have shown that the stress relaxation of 5% polyacrylamide was less than 1%, it is reasonable to assume that the polyacrylamide used is close to a perfectly elastic material in the range of bis-acrylamide concentrations used. Thus, simple Hook's law with only two material variables (Young's modulus and Poisson's ratio) is appropriate for the formulation of the governing equations for the traction force calculation (Section 2.8.1).

4.1.2. Elastic Material Properties

The Young's modulus measured with compressive test (Table 3-1, Fig. 3-3) are very close to the results previously reported by others who used atomic force microscopy (AFM) and tensile

test (Fig. 3-4) (Engler, Bacakova et al. 2004). The Young's modulus was linearly proportional to the crosslinker concentration in range of 0.05% to 0.3%. This result is useful for researchers who want to prepare deformable substrates with different levels of stiffness since the stiffness of the substrate can be estimated easily from the linear interpolation of the result shown in Fig. 3-3.

The compressive tests used to determine the Young's modulus of the polyacrylamide substrate were conducted on 3-D bulk polyacrylamide blocks, which are different in geometry and the surface (no ECM coating) from that of the deformable substrate. However, a previous study (Engler et al., 2004) has demonstrated that the Young's modulus from the ECM-coated thin substrate and that from a bulk block are similar (Fig. 3-4).

4.1.3. Biocompatibility

Although polyacrylamide is generally considered to be inert to the cell, any remaining unpolymerized acrylamide monomer molecules may be toxic, as it is known that acrylamide acts as neurotoxin to cells. Moreover, the initiator and catalyst could also be toxic due to their higher functionality. Therefore, it is important to check that the methods used do not have toxic effects on the cells. The trypan blue stain test, which is one of the standard methods to evaluate cell viability, has confirmed the biocompatibility of the methods used in this study (Section 3.1.3).

4.1.4. Concentration of the Marker Beads

Although spectrophotometer is an optical device usually used to measure the concentration of molecules in the aqueous solutions, the high degree of linear correlation (R^2 value = 0.999) between the optical density and bead concentration proved the applicability of Beer-Lambert law to the beads in polyacrylamide. That is, the bead concentration in the polyacrylamide deformable substrate could be measured accurately with spectrophotometer. This method is

very useful for determining the concentration of the fluorescence beads after the syringe filtering procedure (Section 2.3.3).

The concentration of the beads was used to provide the physical basis to the determination of threshold value in the image processing procedure. In the image processing program, the concentration of the bead would change according to the threshold value applied, so that it is important to determine the threshold value from the experimentally measured bead concentration (Fig. 3-7).

4.1.5. Thickness

The thickness of the polyacrylamide substrate is affected by the osmolarity and temperature of the aqueous environment in the chamber. We have maintained the temperature at 37°C with the temperature control system (Fig. 2-10). We have also maintained the osmolarity for the solutions in the chamber before the cell removal (complete cell culture media) and after (PBS). The osmolarity of both the cell culture media and PBS were measured to be 299 mmol/Kg at 37°C.

As we expected, the thickness of the polyacrylamide substrate determined with image processing technique (Section 3.1.6) after the cell removal was the same as that before the cell removal.

4.1.6. Bead Distribution across the Thickness

As the Z position gets close to the top of the polyacrylamide substrate, the spherical aberration originated from the difference in refractive index (RI) between the polyacrylamide and glass become larger, and the peak intensity of the point spread function (PSF) of point light source drastically decreases (Inoué and Spring 1997). As a result, the signal-to-nose ratio at the

top is lower than those at the bottom (Fig. 4-1C). The resolution decreases as spherical aberration increases. The noises at the top region of the polyacrylamide increase as the signals and contrasts decrease there (Fig. 4-1A). The low signal-to-noise ratio makes it difficult to track the beads at the top region.

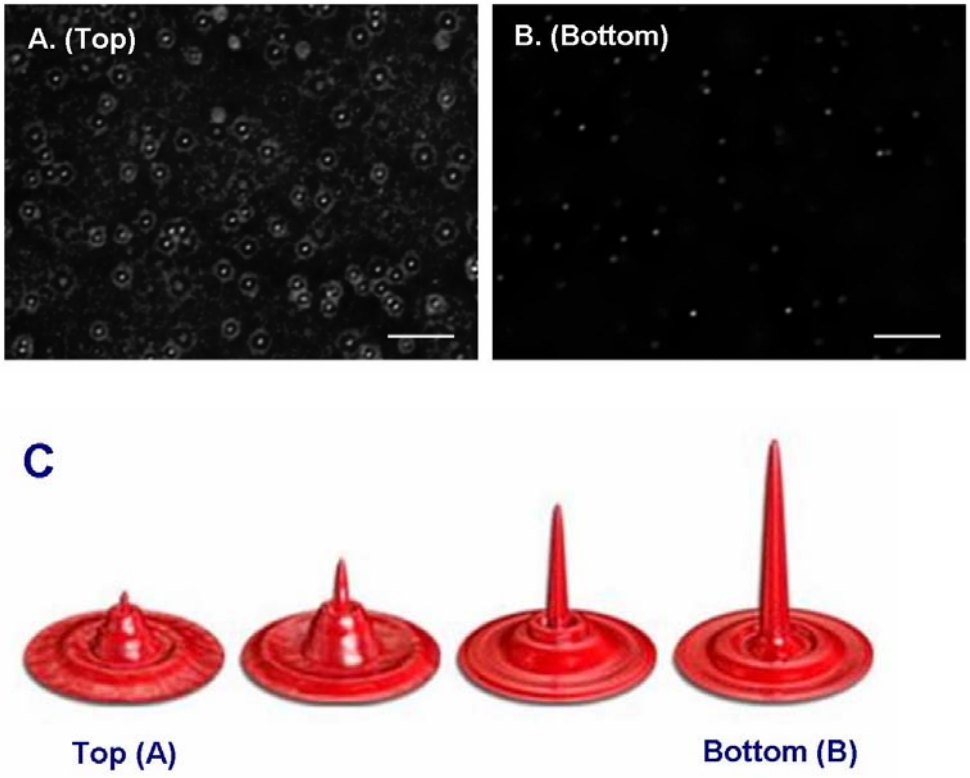

Fig. 4-1. Effect of substrate Z position to PSF and beads images
A: Image of the beads at the top (interface between the cell and substrate)
B: Image of the beads at the bottom (interface between the substrate and glass coverslip) (Bar = 2 μm)
C: Effect of thickness on PSF
(http://www.olympusmicro.com/primer)

The fairly even distribution of beads across the thickness of the polyacrylamide except the top and bottom (Fig. 3-9) verifies that our method can overcome the problems resulting from the spherical aberration.

4.2. Measurement of 3D Displacement of Marker Beads

4.2.1. Comparing the Bead Image Data with Image Processed Results

The image processed results were consistent with the beads displacement data. The tangential displacement field determined (Fig. 3-17A) well represented the bead displacement (Fig. 3-11B). The bead images (Fig. 3-12) indicate zero movement of the beads at the bottom of the polyacrylamide substrate (Table 3-3).

MATLAB coded program, generating top and side views of the bead images and corresponding cell images (Fig. 3-13, Fig. 3-14, and Fig. 3-15), were used to compare the image processed results and image stack. This program supplied a tool for the direct visualization of 3D movement of each bead.

Upward displacement was dominant at the cell edge, and downward displacement was dominant at the cell body (Fig. 3-17B, Fig. 3-21B, and Fig. 3-31 B, D, F, H). Large centripetal tangential displacement is consistent with the results from the previous studies (Fig. 3-17A, Fig. 3-21A, and Fig. 3-31 A, C, E, G) (Pelham and Wang 1997; Balaban, Schwarz et al. 2001; Tan, Tien et al. 2003).

4.2.2. Resolution of Displacement Measurement

It is interesting that the resolution (35.5 nm) of our method was several times smaller than the physical scales (Bead diameter = 200 nm, XY pixel size = 108 nm, Z scan step size = 200 nm), and hence the bead displacement can be measured with a high degree of accuracy.

It should be noted, however, that it is important not only to measure the marker bead displacement accurately but also to have a high density of the marker beads because the displacement field at the position without the marker beads needs to be calculated from the interpolation of the marker beads based on Delaunay triangulation algorithm (Barber, Dobkin et

al. 1996).

4.3. Computational Method to Calculate 3D Traction Force Field

The main difficulty of traction microscopy based on the deformable substrate method is the complex computational procedure needed to compute the traction force field from the measured displacement field. We have developed a simple and effective computation method based on the FEM. Our method gives results with less computation (no supercomputer is needed), and removes many unrealistic assumptions that are required for the previous methods, as will be discussed below. It should be noted that the present method is the first one that gives solution for the 3D problem.

4.3.1 Previous Methods

The traction force calculation procedures in both the polyacrylamide substrate method and the PDMS substrate method were based on the Boussinesq solution (Schwarz, Balaban et al. 2002; Marganski, Dembo et al. 2003). Although the Boussinesq analysis gives analytical solution, it requires assumptions of semi-infinite space and incompressible ($\nu = 0.5$) materials (Landau, Lifshits et al. 1995). Furthermore, Boussinesq solution can only be applicable to 2D problems.

Previous methods contained the inversion procedure of Fredholm equations, which relate strain field with integral equations containing the Green function of stress field. Since the purpose of formulation is to determine stress field from strain field, the Fredholm integral equation should be inversed. But this is not an easy task, because it may cause an ill-posed problem in that the solution is either not unique or not a continuous function of the data. To solve this problem, previous methods needed formidable amounts of computing power, including supercomputer

(Marganski, Dembo et al. 2003) or forced parameter for the regularization procedure (Schwarz, Balaban et al. 2002).

Traction force computational method for PDMS deformable substrate (Balaban, Schwarz et al. 2001) applied the assumption that forces are exerted only at FAs, which significantly reduces the computational complexity. It is unclear whether forces are indeed applied only at FAs because many adherent cells show no detectable FAs (Bray 2001). Furthermore, FA imaging with GFP is subject to the experimental uncertainties due to photobleaching effects, especially for the nascent small FAs which might exert stronger traction forces than mature large FAs (Beningo, Dembo et al. 2001).

4.3.2 Improvements Introduced by the Current Methods

Since deformable substrate thickness is finite, and the Poisson ratio is not 0.5 (Section 2.8.5), these unnecessary assumptions, including infinite half space and incompressible material, have been removed from the present computational method, and this method is applicable to full 3D problems.

Because our method is based on FEM, it can achieve well converged solution with relatively smaller computation power, without forced parameters, nor a-priori assumptions including FAs. The erroneous cyclic boundary conditions for fast Fourier transform (FFT), which is used for the deconvolution of the integral equations, can also be removed.

Increasing number of researchers are interested in the effects of various geometries and substrate materials for studies on live cells in terms of their migration, differentiation, and proliferation. Since FEM is designed for the complex geometry and various material properties, our FEM-based traction force calculation method could be more appropriate and more easily applicable for the 3D substrate or non-elastic substrate materials compared to the previous methods, although previous methods could also be improved for solving 3D problems.

In addition, our FEM-based method is much simpler and easier to use. Although traction force microscopy is getting to be popular, complex traction force computational procedure has limited its utility. Our method is not based on any custom-coded program, but uses ABAQUS which is a widely utilized commercial software for FEM. Many researchers who are not familiar with complex numerical simulations could easily formulate the traction force computation procedure as reported here.

4.4. Role of 3D Traction Force Field in BAEC Migration and FA Dynamics

4.4.1. Tangential Traction Force Field

Tangential force is related to the migration direction and speed of the BAECs. Slowly migrating BAEC (migration speed = 0.168 μm/min) with no polarization (Fig. 3-10, Fig. 3-11) showed a traction force pattern that was even around the edge, and there was not much difference in tangential traction force magnitude between the front and back of the cell along the migration direction (Fig. 3-18A). Fast migrating BAEC (migration speed = 0.468 μm/min) (Fig. 3-19) showed large tangential traction force at the polarized front region compared with the tail region which is retracting (Fig. 3-23A).

The sequence of images including the migration direction (Fig. 3-30 A, C, E) and the tangential traction force pattern (Fig. 3-32 A, C, E) demonstrated that strong tangential forces are exerted at the polarized cell migration front. When the migration speed of the cell is slow (Fig. 3-30 F), the traction force pattern (Fig. 3-32 F) becomes more symmetric compared with that of fast migrating state. The time courses of these experimental results support the interpretations in the paragraph above.

4.4.2. Normal Traction Force Field

Normal traction force is related to the migrating of BAECs, and the magnitude is comparable to that of tangential traction force (Fig. 3-18B, Fig. 3-22B). Upward normal traction force is concentrated at the edge of the cell and downward normal traction force is concentrated under the cell body including the nucleus. Interestingly, the largest downward normal traction force is concentrated at the edge of the cell nucleus (Fig. 3-18B, Fig. 3-22B).

Normal traction force field is related to the FA dynamics of BAECs. FAs with different dynamics show distinct normal traction force patterns. While FAs in new lamella-forming region and retracting region are associated with upward normal traction forces, FAs under the cell body are associated with downward normal forces (Section 3.2.5 and Section 3.3.4).

These results indicate that normal traction forces might play an important role in the FA dynamics including FA turnover and FA stabilization or maturation. It has been reported that traction force is required for the stabilization and maturation of FAs. It is still unclear, however, why the FAs at the cell front and cell rear show different behaviors even though they experience similar tangential traction force. The differential patterns of normal traction force could be the answer to explain these findings. Downward normal traction forces might help to stabilize the FAs, but upward normal force might tend to unstabilize and turn over the FAs.

V. CONCLUSIONS

Mechanical forces play an important role in the regulation of physiological responses which affect cell structure and function, including local changes of adhesion sites and cytoskeletons, and alterations in cell motility, proliferation and survival. The traction forces exerted by an adherent cell on the substrate have been studied with the traction force microscopy technique. Previous studies, have considered only two-dimensional (2D) traction forces tangential to the substrate, although these forces are three-dimensional (3D) in nature.

I have developed a novel 3D traction force microscopy technique to measure the 3D traction forces, including the normal traction force, of live cells using the polyacrylamide deformable substrate method. The polyacrylamide deformable substrate was characterized, including its materials properties, biocompatibilities, and marker bead concentrations. To obtain the displacement field from the 3D image stack acquired from a confocal microscope, image processing programs were coded with MATLAB and their applicabilities and resolution were determined. I have also developed an improved 3D computational method to compute the traction forces based on the FEM. This method has shown better performance in comparison to the methods used in previous studies.

I have applied this novel method to BAEC to determine 3D traction forces, including the normal force, and their relations with BAEC migration and FA dynamics. The results demonstrated that not only tangential, but also normal, traction forces are exerted by the BAEC on the substrate. Upward normal traction force is found at the edge of the BAEC, while downward normal traction force is dominant under the nucleus. Combined with the green fluorescent protein (GFP) technique to visualize the focal adhesion (FA) molecules, including focal adhesion kinase (FAK) and paxillin, it has been demonstrated that 3D traction forces are related to the FA dynamics of BAECs. It has been shown that upward normal traction force is

related to the dynamic FAs (FAs moving over long distance or undergoing turnover), and that downward normal traction force is related to the stable FAs (FAs do not change their position and size) during the cell migration.

The application of this 3D traction force microscopy technique to BAECs and other types of cells provides a new way of elucidating the full range of biomechanical dynamics of cells in conjunction with their biochemical activities and can contribute to the understanding of cellular functions in health and disease.

VI. REFERENCES

Alberts, B. (2002). Molecular biology of the cell. New York, Garland Science.

Aplin, J. D. and R. C. Hughes (1981). "Protein-derivatised glass coverslips for the study of cell-to substratum adhesion." Anal Biochem **113**(1): 144-8.

Balaban, N. Q., U. S. Schwarz, et al. (2001). "Force and focal adhesion assembly: a close relationship studied using elastic micropatterned substrates." Nat Cell Biol **3**(5): 466-72.

Barber, C. B., D. P. Dobkin, et al. (1996). "The Quickhull algorithm for convex hulls." Acm Transactions on Mathematical Software **22**(4): 469-483.

Beningo, K. A., C. M. Lo, et al. (2002). "Flexible polyacrylamide substrata for the analysis of mechanical interactions at cell-substratum adhesions." Methods Cell Biol **69**: 325-39.

Beningo, K. A., M. Dembo, et al. (2001). "Nascent focal adhesions are responsible for the generation of strong propulsive forces in migrating fibroblasts." J Cell Biol **153**(4): 881-8.

Bershadsky, A. D., N. Q. Balaban, et al. (2003). "Adhesion-dependent cell mechanosensitivity." Annu Rev Cell Dev Biol **19**: 677-95.

Bray, D. (2001). Cell movements : from molecules to motility. New York, Garland Pub.

Burton, K., J. H. Park, et al. (1999). "Keratocytes generate traction forces in two phases." Mol Biol Cell **10**(11): 3745-69.

Burton, K. and D. L. Taylor (1997). "Traction forces of cytokinesis measured with optically modified elastic substrata." Nature **385**(6615): 450-4.

Chen, C. S., J. Tan, et al. (2004). "Mechanotransduction at cell-matrix and cell-cell contacts." Annu Rev Biomed Eng **6**: 275-302.

Chien, S. (2007). "Mechanotransduction and endothelial cell homeostasis: the wisdom of the cell." Am J Physiol Heart Circ Physiol **292**(3): H1209-24.

Cukierman, E., R. Pankov, et al. (2001). "Taking cell-matrix adhesions to the third dimension." Science **294**(5547): 1708-12.

Engler, A., L. Bacakova, et al. (2004). "Substrate compliance versus ligand density in cell on gel responses." Biophys J **86**(1 Pt 1): 617-28.

Galbraith, C. G. and M. P. Sheetz (1998). "Forces on adhesive contacts affect cell function." Curr Opin Cell Biol **10**(5): 566-71.

Harris, A. K., P. Wild, et al. (1980). "Silicone rubber substrata: a new wrinkle in the study of cell locomotion." Science **208**(4440): 177-9.

Inoué, S. and K. R. Spring (1997). Video microscopy : the fundamentals. New York, Plenum Press.

Kaverina, I., O. Krylyshkina, et al. (2000). "Enforced polarisation and locomotion of fibroblasts lacking microtubules." Curr Biol **10**(12): 739-42.

Landau, L. D., E. M. Lifshits, et al. (1995). Theory of elasticity. Oxford ; Boston, Butterworth-Heinemann.

Li, C., Z. Hu, et al. (1993). "Poisson's ratio in polymer gels near the phase-transition point." Physical Review. E. Statistical Physics, Plasmas, Fluids, and Related Interdisciplinary Topics **48**(1): 603-606.

Li, S., B. P. Chen, et al. (1999). "Distinct roles for the small GTPases Cdc42 and Rho in endothelial responses to shear stress." J Clin Invest **103**(8): 1141-50.

Li, S., J. L. Guan, et al. (2005). "Biochemistry and biomechanics of cell motility." Annu Rev Biomed Eng **7**: 105-50.

Lo, C. M., H. B. Wang, et al. (2000). "Cell movement is guided by the rigidity of the substrate." Biophys J **79**(1): 144-52.

Marganski, W. A., M. Dembo, et al. (2003). "Measurements of cell-generated deformations on flexible substrata using correlation-based optical flow." Methods Enzymol **361**: 197-211.

Munevar, S., Y. Wang, et al. (2001). "Traction force microscopy of migrating normal and H-ras transformed 3T3 fibroblasts." Biophys J **80**(4): 1744-57.

Munevar, S., Y. L. Wang, et al. (2001). "Distinct roles of frontal and rear cell-substrate adhesions in fibroblast migration." Mol Biol Cell **12**(12): 3947-54.

Nelson, C. M., R. P. Jean, et al. (2005). "Emergent patterns of growth controlled by multicellular form and mechanics." Proc Natl Acad Sci U S A **102**(33): 11594-9.

Nicolas, A., B. Geiger, et al. (2004). "Cell mechanosensitivity controls the anisotropy of focal adhesions." Proc Natl Acad Sci U S A **101**(34): 12520-5.

Odian, G. G. (2004). Principles of polymerization. Hoboken, N.J., Wiley-Interscience.

Oliver, T., M. Dembo, et al. (1998). "Measurement of traction forces in cells locomoting along a substratum. Video supplement." Cell Motil Cytoskeleton **39**(4): 342-4.

Paszek, M. J., N. Zahir, et al. (2005). "Tensional homeostasis and the malignant phenotype." Cancer Cell **8**(3): 241-54.

Pelham, R. J., Jr. and Y. Wang (1997). "Cell locomotion and focal adhesions are regulated by substrate flexibility." Proc Natl Acad Sci U S A **94**(25): 13661-5.

Pelham, R. J., Jr. and Y. Wang (1999). "High resolution detection of mechanical forces exerted by

locomoting fibroblasts on the substrate." Mol Biol Cell **10**(4): 935-45.

Ridley, A. J. and A. Hall (1992). "The small GTP-binding protein rho regulates the assembly of focal adhesions and actin stress fibers in response to growth factors." Cell **70**(3): 389-99.

Riveline, D., E. Zamir, et al. (2001). "Focal contacts as mechanosensors: externally applied local mechanical force induces growth of focal contacts by an mDia1-dependent and ROCK-independent mechanism." J Cell Biol **153**(6): 1175-86.

Schwarz, U. S., N. Q. Balaban, et al. (2002). "Calculation of forces at focal adhesions from elastic substrate data: the effect of localized force and the need for regularization." Biophys J **83**(3): 1380-94.

Shemesh, T., B. Geiger, et al. (2005). "Focal adhesions as mechanosensors: a physical mechanism." Proc Natl Acad Sci U S A **102**(35): 12383-8.

Tan, J. L., J. Tien, et al. (2003). "Cells lying on a bed of microneedles: an approach to isolate mechanical force." Proc Natl Acad Sci U S A **100**(4): 1484-9.

Vogel, V. and M. Sheetz (2006). "Local force and geometry sensing regulate cell functions." Nat Rev Mol Cell Biol **7**(4): 265-75.

Weiss, P. and A. Moscona (1958). "Type-specific morphogenesis of cartilages developed from dissociated limb and scleral mesenchyme in vitro." J Embryol Exp Morphol **6**(2): 238-46.

Zaidel-Bar, R., M. Cohen, et al. (2004). "Hierarchical assembly of cell-matrix adhesion complexes." Biochem Soc Trans **32**(Pt3): 416-20.